

Kinematic scaling relations of disc galaxies from ionised gas at $z \sim 1$ and their connection with dark matter halos

Pavel E. Mancera Piña^{1,★}, Enrico M. Di Teodoro², S. Michael Fall³, Antonino Marasco⁴,
Mariska Kriek¹, and Marco Martorano⁵.

¹ Leiden Observatory, Leiden University, P.O. Box 9513, 2300 RA, Leiden, The Netherlands

² Dipartimento di Fisica e Astronomia, Università degli Studi di Firenze, via G. Sansone 1, 50019 Sesto Fiorentino, Firenze, Italy

³ Department of Physics and Astronomy, Johns Hopkins University, 3400 N. Charles Street, Baltimore, MD 21218, USA

⁴ INAF – Padova Astronomical Observatory, Vicoletto dell’Osservatorio 5, I-35122 Padova, Italy

⁵ Sterrenkundig Observatorium, Universiteit Gent, Krijgslaan 281 S9, 9000 Gent, Belgium

ABSTRACT

We derive the Tully–Fisher (TFR, $M_* - V_{\text{circ}}$) and Fall (FR, $j_* - M_*$) relations at redshift $z = 0.9$ using a sample of 43 main-sequence disc galaxies with $\text{H}\alpha$ IFU data and JWST/HST imaging. The strength of our analysis lies in the use of state-of-the-art 3D kinematic models to infer galaxy rotation curves, the inclusion and morphological modelling of NIR bands, and the use of SED modelling applied to our photometry measurements to estimate stellar masses. After correcting the inferred $\text{H}\alpha$ velocities for asymmetric drift, we find a TFR of the form $\log(M_*/M_\odot) = a \log(V_{\text{circ},\text{f}}/150 \text{ km s}^{-1}) + b$, with $a = 3.82^{+0.55}_{-0.40}$ and $b = 10.27^{+0.06}_{-0.07}$, as well as a FR of the form $\log(j_*/\text{kpc km s}^{-1}) = a \log(M_*/10^{10.5} M_\odot) + b$, with $a = 0.44^{+0.06}_{-0.06}$ and $b = 2.86^{+0.02}_{-0.02}$.

When compared to their $z = 0$ counterparts, we find moderate evolution in the TFR and strong evolution in the FR over the past 8 Gyr. We interpret our findings in the context of the galaxy-to-halo scaling parameters $f_M = M_*/M_{\text{vir}}$ and $f_j = j_*/j_{\text{vir}}$. We infer that at $z = 0.9$ both f_M and f_j are higher and less mass-dependent than at $z = 0$. We speculate that the evolution of f_j can be driven by more efficient and centrally concentrated stellar feedback at $z = 0.9$, or by an appreciable dry merger history. We also show that assuming the galaxies populating our $z = 0.9$ relations evolve into those populating the $z = 0$ relations leads to an apparent discrepancy with the hierarchical growth of dark matter halos. To solve this issue, one needs to evoke a progenitor bias scenario, unknown systematics affecting our and previous measurements, or consider the possibility that $\text{H}\alpha$ kinematics is not a reliable dynamical tracer.

Key words. galaxies: kinematics and dynamics – galaxies: formation – galaxies: evolution – galaxies: high-redshift – galaxies: star formation – galaxies: fundamental parameters

1. Introduction

Two of the most fundamental scaling relations for disc galaxies are those connecting their stellar mass (M_*) with their rotational velocities (V) and their stellar specific angular momentum (j_*), i.e. the stellar Tully–Fisher (TFR, Tully & Fisher 1977; Bell & de Jong 2001) and Fall (FR, Fall 1983) relations. These scaling relations are closely intertwined with the process of galaxy evolution. According to our current galaxy formation theories, dark matter and baryons acquire their angular momentum due to tidal torques from neighbouring systems before virialisation. Upon the dissipation and gravitational collapse of the baryons, the global angular momentum is approximately conserved, leading the baryons in disc galaxies to settle into relatively thin, disc-like structures supported by rotation, and embedded in more extended dark matter haloes without significant rotational support (e.g. Peebles 1969; Binney 1977; White & Rees 1978; Fall & Efstathiou 1980; Blumenthal et al. 1984; White 1984; Dalcanton et al. 1997; Mo et al. 1998). In this way, the distribution of angular momentum is thought to set the rotational velocity and mass distribution of galaxies, regulating also their morphology and gas content (e.g. Romanowsky & Fall 2012; Obreschkow & Glazebrook 2014; Cortese et al. 2016; Lagos et al. 2017; Swinbank et al. 2017; Sweet et al. 2020; Mancera Piña et al. 2021b;

Geesink et al. 2025). Observational constraints on the TFR and FR provide crucial benchmarks for galaxy formation models.

In the nearby Universe, at $z \sim 0$, the TFR and FR have been studied in detail and are found to be well described by unbroken power laws of the form $M_* \propto V^a$ and $j_* \propto M_*^a$, respectively. These slopes are found to be $a \approx 3.5 - 5$ for the TFR (e.g. Bell & de Jong 2001; Reyes et al. 2011; Ponomareva et al. 2017; Catinella et al. 2023; Marasco et al. 2025) and $a \approx 0.5 - 0.6$ for the FR (e.g. Posti et al. 2018; Mancera Piña et al. 2021a; Hardwick et al. 2022; Di Teodoro et al. 2021, 2023; Marasco et al. 2025). At higher redshifts, the situation remains significantly less certain. Although different works have studied the TFR and FR up to $z \sim 2.5$ (e.g. Conselice et al. 2005; Cresci et al. 2009; Burkert et al. 2016; Contini et al. 2016; Di Teodoro et al. 2016; Price et al. 2016; Harrison et al. 2017; Swinbank et al. 2017; Gillman et al. 2019; Marasco et al. 2019; Sweet et al. 2019; Pelliccia et al. 2019; Tiley et al. 2019; Mercier et al. 2023), there is no consensus on whether or not the relations (slopes, intercept, intrinsic scatter) evolve with z (see Übler et al. 2017; Pelliccia et al. 2019; Bouché et al. 2021; Sharma et al. 2024; Espejo Salcedo et al. 2025). Some of the difficulty in tracing the evolution of the TFR and FR arises from observational uncertainties and methodological limitations when studying high- z disc galaxies. Two major concerns in most previous works are the derivation of galaxy kinematics and of stellar masses. Obtaining reliable kinematics at high z is challenging, due to both the limited quality of

* e-mail: pavel@strw.leidenuniv.nl

the data (low spatial resolution, low signal-to-noise ratio, short radial extent) and the intrinsically complex structure of young galaxies. In addition, M_* is typically estimated through spectral energy distribution (SED) fitting (or by adopting a fixed mass-to-light ratio), often relying on photometry of variable quality and lacking rest-frame near-infrared (NIR) coverage, which is crucial for constraining the underlying stellar mass distribution.

In this work, we revisit the evolution of the TFR and FR at $z \sim 1$ while addressing these limitations. In particular, our study improves upon previous efforts in several key ways. *i*) We use well-tested software that takes into account observational effects for data of limited quality in a self-consistent way. *ii*) We exploit new JWST observations providing exquisite NIR data, improving the stellar mass density profiles. *iii*) We apply asymmetric drift corrections to take into account the pressure-supported motions of ionised gas and stars compared to cold gas (which is typically used at $z = 0$); this is crucial as it is a systematic effect that depends on M_* . *iv*) Rather than assuming stellar-to-halo mass and specific angular momentum ratios that depend on abundance-matching calibrations, we show that these can be directly derived from the observed TFR and FR. *v*) Finally, we assess the evolution of the TFR and FR at $z \sim 1$ by contrasting against new and improved $z = 0$ determinations (Marasco et al. 2025). Throughout this work, we adopt a Λ CDM cosmology with $\Omega_{m,0} = 0.3$, $\Omega_{\Lambda,0} = 0.7$, and $H_0 = 70 \text{ km s}^{-1} \text{ Mpc}^{-1}$.

2. Data and sample selection

For this study, we make use of data tracing the resolved stellar mass distribution and kinematics of galaxies at $z \approx 1$. For the kinematics, we rely on the Integral Field Unit (IFU) spectroscopy from the KROSS (Stott et al. 2016) and KMOS^{3D} (Wisnioski et al. 2015) surveys. These surveys mapped the H α distribution and kinematics of galaxies at $z \sim 0.6 - 2.5$ using the KMOS instrument at the VLT. The spectral resolution of the data is $R = \lambda/\Delta\lambda \sim 3500 - 4000$, which for H α at our z corresponds to $\sigma \sim 40 \text{ km/s}$. The typical FWHM of the PSF is $\sim 0.5 - 0.8$ arcsec (Stott et al. 2016; Wisnioski et al. 2019). We note that the kinematics of these samples have been studied before (e.g. Stott et al. 2016; Burkert et al. 2016; Harrison et al. 2017; Übler et al. 2017; Tiley et al. 2019; Sharma et al. 2021), although with different approaches from ours, as discussed below.

For this work, we require a galaxy sample that meets several selection criteria on the kinematic data. We start by visually inspecting all the position-velocity (PV) slices along the major and minor axes of the galaxies in the parent sample, keeping only those systems with high signal-to-noise (S/N) and compelling regular kinematics (i.e., clear velocity gradients in the major-axis PV, no gradients in the minor-axis PV, no signs of mergers) to ensure a clean sample of rotating discs. Next, we select against poorly resolved galaxies with H α emission less extended than ~ 2 times the PSF. As shown below, we verified that this criterion does not appear to significantly bias the mass-size relation of our galaxies, which is consistent with literature relations for the star-forming disc population.

In addition, we require that the galaxies have available HST- or JWST-based morphological Sérsic models. Specifically, we rely on the results from van der Wel et al. (2012); Martorano et al. (2024), and Martorano et al. (2025, submitted), who carefully built PSFs and used GALFIT (Peng et al. 2010, see Martorano et al. 2023 for the treatment of the uncertainties) to obtain accurate effective radii ($R_{\text{eff},*}$), Sérsic indices (n), position angles, and axial ratios (b/a). We prioritise the parameters obtained from the reddest available band, which is f444w from NIRCam on JWST

for 60% of our final sample (see below), and f160w from WFC3 on HST for the remaining 40%. These parameters and our M_* estimates (described next) define $\Sigma_*(R)$, our stellar-mass surface-density profiles. We note that at our redshifts, f160w and f444w trace rest-frame emission at $0.81 \mu\text{m}$ and $2.33 \mu\text{m}$, respectively, roughly corresponding to the rest-frame I - and K -bands. At our redshift and M_* range, galaxy sizes in these bands agree within 10 – 20% (van der Wel et al. 2014; Suess et al. 2022).

A key aspect of this study is the use of robust M_* estimates, which we obtain using the SED fitting approach by Marasco et al. (2025) and exploiting the HST (ACS or WFC3) and/or JWST (NIRCam) photometry. In particular, we use the publicly available images from the following surveys: CANDELS (Grogin et al. 2011; Koekemoer et al. 2011), COSMOS (Koekemoer et al. 2007; Scoville et al. 2007), PRIMER (Dunlop et al. 2021), JADES (Eisenstein et al. 2023), and COSMOS-Web (Casey et al. 2023). These surveys provide imaging in (some of) the following filters: f444w, f356w, f277w, f150w, f115w, and f090w from JWST, and f160w, f125w, f105w, f814w, f850lp, and f606w from HST. Using only space-based imaging (a condition not always imposed in previous studies) is crucial, as it has significantly better spatial resolution, photometric calibration and overall image quality than ground-based data. Moreover, unlike previous studies, we use JWST rest-frame bands, allowing us to characterise the stellar masses of our sample better. We carefully extract the photometry (see Marasco et al. 2025 for full details) in the available bands and model the SED with the software BAGPIPES (Carnall et al. 2018), adopting ‘non-parametric’ star-formation histories and considering the stellar population models from Charlot & Fall (2000, 2016 version¹), and a Kroupa (2002) IMF. The redshift is fixed to the H α value from the KROSS and KMOS^{3D} surveys. We only consider galaxies with fluxes in at least four bands (we typically have five or six bands, and up to ten) and whose model SEDs provide a high-quality fit to the data ($p(>\chi^2) > 0.05$, see Marasco et al. 2025). Marasco et al. (2025) showed that their SED-based and dynamical M_* estimates in local disc galaxies (e.g. Posti et al. 2019a; Schombert et al. 2022; Mancera Piña et al. 2025) agree within ~ 0.2 dex across nearly six orders of magnitude in M_* , which implies that they can be used interchangeably in the study of scaling relations and their evolution.

Assuming an intrinsic disc axial ratio $q_0 = 0.2$ (e.g. Fouque et al. 1990), we derive galaxy inclinations from the observed b/a using the standard (Hubble 1926) relation $\cos^2(i) = ((b/a)^2 - q_0^2)/(1 - q_0^2)$. We exclude galaxies with $i < 30^\circ$ (where small errors in i cause significant velocity uncertainties) and $i > 80^\circ$ (for which ring-by-ring kinematic models are not well-suited due to the overlap of different lines of sight). From the remaining sample, we retain only systems for which 3D kinematics can be reliably modelled. For this, we use the forward-modelling software ^{3D}Barolo (Di Teodoro & Fraternali 2015), which accounts for beam smearing and enables robust recovery of intrinsic rotation curves and velocity dispersions. Full details of the kinematic modelling are provided in Appendix A.

After applying our selection criteria, we end up with a set of 43 disc galaxies. Our sample spans the range $0.78 < z < 1.03$ with a median z of 0.89. This redshift range corresponds to cosmic ages between 6.7 Gyr and 5.6 Gyr. The galaxies have stellar masses in the range $5 \times 10^9 < M_*/M_\odot < 2 \times 10^{11}$. Given

¹ We have also explored the BPASS stellar population models (Eldridge & Stanway 2009; Stanway & Eldridge 2018), finding that they produce stellar masses lower 0.25 dex on average, by but without significant systematics, and therefore not affecting the slopes of the scaling relations presented in Sect. 4.1.

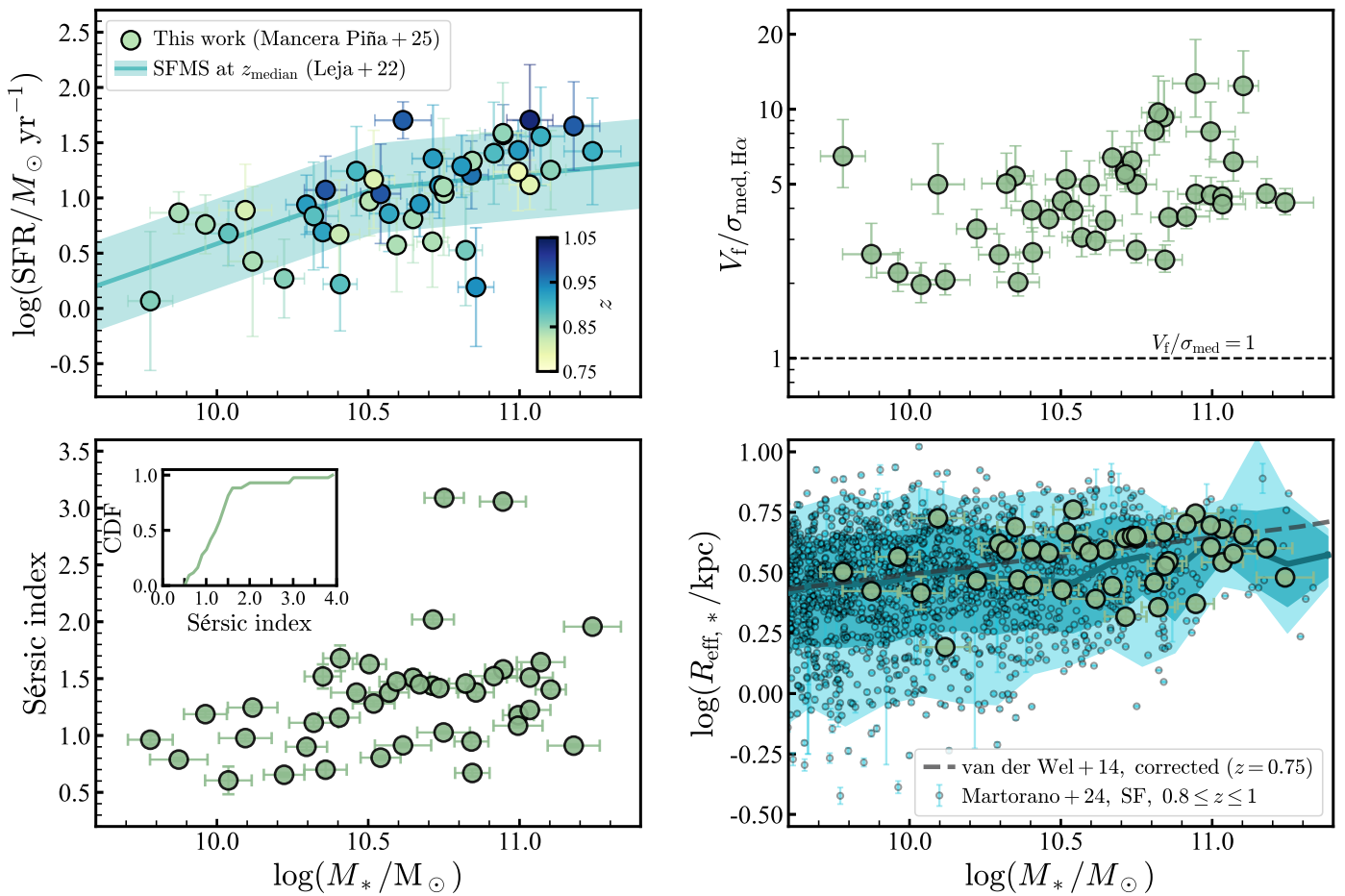


Fig. 1: *Top left*: SFMS defined by our high- z galaxies, colour-coded by their redshift. The reference SFMS from Leja et al. (2022) is shown. SFRs come from our SED fitting. *Top right*: Rotation to dispersion ratio for our galaxy sample. *Bottom left*: Sérsic index as a function of M_* . The inset shows the cumulative distribution of the Sérsic indices. *Bottom right*: Stellar mass-size relation. Our galaxies (green markers) are contrasted against 1) the individual measurements from Martorano et al. (2024) at $0.8 \leq z \leq 1$ (blue markers) and their 1 and 2σ ranges (blue bands), and 2) the relation from van der Wel et al. (2014) at $z = 0.75$ after applying approximate corrections to account for the sizes differences in optical vs. NIR bands.

all our selection cuts based on data quality, establishing a selection function is far from straightforward. However, we find that our final sample is representative of the typical star-forming galaxy population, characterised by regular kinematics. This is illustrated in Fig. 1, showing that the sample follows the star formation main sequence (SFMS, top left panel) at $z \approx 0.9$, is dominated by rotation² (top right panel), has a Sérsic index distribution typical of discs (median $n \approx 1.3$, bottom left panel), and follows the $M_* - R_{\text{eff},*}$ relation from Martorano et al. (2024) at $z = 0.9$ and van der Wel et al. (2014) at $z = 0.75$ (bottom right panel³). Table D.1 lists the main properties of our sample.

² Our median rotation-to-dispersion ratio $V_f/\sigma_{H\alpha, \text{med}}$ is close to 5 (see Appendix A), where $\sigma_{H\alpha, \text{med}}$ is the median $H\alpha$ velocity dispersion radial profile. Since $\sigma_{H\alpha}$ is typically twice that of the cold gas (Levy et al. 2018; Girard et al. 2021; Ejdetjärn et al. 2022), this correction would align $V_f/\sigma_{H\alpha, \text{med}}$ with typical values observed at $z = 0$ in disc galaxies with cold gas kinematics (e.g. Mancera Piña et al. 2025).

³ We have modified the relation from van der Wel et al. (2014) to account for typical differences between their optical sizes and NIR sizes (used in Martorano et al. 2024 and this work). Specifically, we rescaled the optical sizes by linear interpolation so that they decrease by 0.1 dex at $\log(M_*/M_\odot) = 9.5$ and by 0.22 dex at $\log(M_*/M_\odot) = 11.3$, consistent with Martorano et al. (2024, see their Fig. 7).

3. Estimating $V_{\text{circ},f}$ and j_*

Our kinematic modelling described in Appendix A allows us to obtain the intrinsic rotational velocity of the ionised gas ($V_{H\alpha}(R)$) and its velocity dispersion ($\sigma_{H\alpha}(R)$). Instead, the TFR requires the circular speed (V_{circ} ⁴), and the FR requires the stellar rotational velocities (V_*). If derived from cold gas (e.g. H I or CO), the rotational velocities could be used directly to build the TFR and FR, since the cold gas has a high rotational support and low pressure-supported motions, and the rotational speeds are close to both V_{circ} and V_* (at least for $M_* \gtrsim 5 \times 10^8 M_\odot$, see Mancera Piña et al. 2021a). However, for ionised gas at $z \sim 1$ (see also Catinella et al. 2023 at $z = 0$) the velocity dispersions tend to be higher and the rotation-to-dispersion ratios lower, making it imperative to correct for the different asymmetric drift of the stars and ionised gas. In particular, V_{circ} , V_* , and our measured $V_{H\alpha}$ are related through the expressions

$$V_{\text{circ}}^2 = V_{H\alpha}^2 + V_{\text{AD}, H\alpha}^2, \quad (1)$$

⁴ $V_{\text{circ}}(R)$ is the speed of a test particle in pure circular orbit at radius R , e.g. Binney & Tremaine (2008); Cimatti et al. (2019). V_{circ} is close to the rotational speed of H I , typically used at $z = 0$ to derive the TFR.

$$V_*^2 = V_{\text{circ}}^2 - V_{\text{AD},*}^2, \quad (2)$$

where $V_{\text{AD},*}$ and $V_{\text{AD},\text{H}\alpha}$ are the asymmetric drift (AD) corrections to account for the pressure support provided by the stars and the ionised gas, respectively. Therefore, the steps to follow are first to convert our $V_{\text{H}\alpha}$ into V_{circ} , and then V_{circ} into V_* . We note that in this study, all uncertainties are propagated throughout our calculations using Monte Carlo sampling (with measurement errors assumed to be Gaussian). The quoted errors correspond to the difference between the 84th and 16th percentiles and are propagated using the full sampling of the posterior distributions.

Under the assumptions of constant scale heights and relatively thin discs, the AD corrections (Binney & Tremaine 2008) take the approximate form

$$V_{\text{AD}}^2(R) = -R \left(\frac{\sigma_z(R)}{\beta} \right)^2 \frac{\partial \ln(\Sigma(R) \sigma_z(R)^2)}{\partial R}, \quad (3)$$

with Σ the ionised gas or stellar surface density, and $\beta \equiv \sigma_z/\sigma_R$, with σ_z and σ_R the vertical and radial components of the stellar or ionised gas velocity dispersion profiles.

We start by computing $V_{\text{AD},\text{H}\alpha}$. For this, we make the common assumption that the gas velocity dispersion is isotropic, which sets $\beta = 1$. Next we assume a constant $\sigma_{z,\text{H}\alpha}(R)$, given by the median value of our observed $\sigma_{\text{H}\alpha}$ ⁵. Concerning the spatial distribution, while in principle we have access to $\Sigma_{\text{H}\alpha}$, the spatial resolution of the $\text{H}\alpha$ data is too low to infer detailed radial profiles. Instead, we assume that $\text{H}\alpha$ shares the same Sérsic index as the stellar disc, but with $R_{\text{eff},\text{H}\alpha} = 1.13(\pm 0.05) R_{\text{eff},*}$, as found for disc galaxies within our M_* and z range (Nelson et al. 2016; Wilman et al. 2020). With this $V_{\text{AD},\text{H}\alpha}$, we can convert $V_{\text{H}\alpha}$ into V_{circ} .

Kinematic data at $z \sim 0$ have extended H_I data that can be traced far out the disc with many resolution elements to measure the characteristic flat velocity of $V_{\text{circ}}(R)$ ($V_{\text{circ},\text{f}}$), which we need for the TFR. In contrast, high- z rotation curves have more limited resolution (typically three to five (nearly) independent resolution elements, see Appendix A) and do not extend as much as H_I, which prevents us from performing the same measurement. Instead, we implement the following approach. We first fit $V_{\text{circ}}(R)$ with the arctan rotation curve model from Courteau et al. (2007), i.e. $V_{\text{circ}}(R) = (2/\pi) V_a \arctan(R/r_t)$, with V_a the asymptotic velocity of the rotation curve and r_t a turnover radius between the rising and outer part of the rotation curve. In practice, the fit is done using the Bayesian Nested Sampling software *dynesty* (Speagle 2020), minimising a χ^2 likelihood. From empirical tests using a sample of $z = 0$ disc galaxies with high-resolution kinematics (described in Appendix B), we find that we can estimate $V_{\text{circ},\text{f}}$ with a $\sim 1\%$ accuracy, by evaluating the best-fit arctan model at $R = 2 R_{\text{eff},*}$ for galaxies with $V_a \geq 100 \text{ km/s}$, (as those in our high- z sample), and at $R = 3 R_{\text{eff},*}$ for lower V_a . From this, we obtain the $V_{\text{circ},\text{f}}$ needed for the TFR.

Next, we focus on $V_{\text{AD},*}$, which will allow us to estimate V_* for the FR. We follow the procedure detailed in Mancera Piña et al. (2021a). Specifically, as supported by theoretical and observational work at $z = 0$ (van der Kruit 1988; Martinsson et al.

⁵ We do this for simplicity and to avoid over-interpreting the data: for some galaxies, $\sigma_{\text{H}\alpha}(R)$ may not be smooth and show discontinuities driven by the limited S/N and resolution of the observations. In any case, we have corroborated that using the actual $\sigma_{\text{H}\alpha}(R)$ profile does not affect significantly the results presented below.

2013), we consider that the stellar velocity dispersion profile has a radial profile of the form

$$\sigma_{z,*}(R)/\text{km s}^{-1} = \max[\sigma_{z,0,*} \exp(-R/1.19R_{\text{eff},*}), 10], \quad (4)$$

with an empirical $\sigma_{z,0,*}$ derived by Mancera Piña et al. (2021a) based on measurements of disc galaxies at $z = 0$ (see also e.g. Martinsson et al. 2013) given by

$$\frac{\sigma_{z,0,*}}{\text{km s}^{-1}} = 9.7 \left(\frac{V_{\text{circ},\text{f}}}{100 \text{ km s}^{-1}} \right)^2 + 2.6 \left(\frac{V_{\text{circ},\text{f}}}{100 \text{ km s}^{-1}} \right) + 10.61(\pm 5), \quad (5)$$

which we assume not to evolve with z . The above calibrations are semi-empirical, but it is worth to note that detailed measurements show some degree of diversity among galaxies (Mogotsi & Romeo 2019). Finally, we consider $\beta = 0.8 \pm 0.2$, consistent with the values found for nearby disc galaxies by Mogotsi & Romeo (2019). With all of the above, we compute $V_{\text{AD},*}$ and convert V_{circ} into V_* .

With V_* , we can determine j_* , which is defined as

$$j_* = \frac{2\pi \int R'^2 \Sigma_*(R') V_*(R') dR'}{2\pi \int R' \Sigma_*(R') dR'}. \quad (6)$$

For $z = 0$ data, Eq. 6 is computed by summing the high-resolution rotation curves and mass profiles (e.g. Posti et al. 2018; Mancera Piña et al. 2021a; Di Teodoro et al. 2023). For the $z = 0.9$ data, we rely on our Sérsic models for Σ_* and on new arctan fits for $V_*(R)$. We integrate Eq. 6 up to $R_{\text{out}} = 10 R_{\text{eff}}$, ensuring the convergence of j_* . As detailed in Appendix B, we have tested our procedure on a comparison sample at $z = 0$, finding that j_* is recovered with a $\sim 5\%$ accuracy.

Before delving into the best-fitting TFR and FR implied by our measurements, we would like to emphasise the importance of implementing AD corrections when dealing with ionised gas kinematics, which is often overlooked when studying the TFR and FR at high- z . As mentioned before, applying such corrections is key to account for the varying rotation-to-dispersion ratios arising from various kinematic tracers at different redshifts, which are also a function of M_* since typically low-mass galaxies have less rotational support (Fig. 1). To illustrate this, we quote the average differences in $\log(V_{\text{circ},\text{f}})$ and $\log(j_*)$ for our galaxy sample implementing or not the AD corrections. At $\log(M_*/M_\odot) = 10, 10.5$, and 11 , the AD-corrected values for $\log(V_{\text{circ},\text{f}})$ are typically higher by about 0.09 dex, 0.04 dex, and 0.02 dex, respectively. Similarly, at the same masses, the AD-corrected values for $\log(j_*)$ are higher by about 0.05 dex, 0.02 dex, and 0.0 dex, on average. As we discuss in the next section, these offsets are large enough to impact the best-fitting TFR and FR.

4. Scaling relations

4.1. Scaling laws at $z = 0.9$

In Fig. 2, we show our measurements in the $M_* - V_{\text{circ},\text{f}}$ and $j_* - M_*$ planes. As found at low- z , our high- z galaxies follow well-defined sequences of increasing $V_{\text{circ},\text{f}}$ and j_* with increasing M_* . In Fig A.3, we show that at fixed M_* galaxies with a high $V_{\text{f}}/\sigma_{\text{med}}$ also have a high $V_{\text{circ},\text{f}}$ and j_* . We parametrise the observed distributions in the $M_* - V_{\text{circ},\text{f}}$ and $j_* - M_*$ planes with power-law models of the form

$$\log \left(\frac{M_*}{M_\odot} \right) = a \log \left(\frac{V_{\text{circ},\text{f}}}{150 \text{ km s}^{-1}} \right) + b, \quad (7)$$

$$\log\left(\frac{j_*}{\text{kpc km s}^{-1}}\right) = a \log\left(\frac{M_*}{10^{10.5} M_\odot}\right) + b, \quad (8)$$

where a is the slope of the relation and b is the intercept at our pivot mass and velocity. The pivot values of $10^{10.5} M_\odot$ and 150 km/s, chosen to be relatively close to the median values for our high- z sample, help in reducing the covariance between slopes and intercepts. In practice, the power-law fits to our TFR and FR are obtained using `dynesty`, adding an extra term to allow for intrinsic scatter perpendicular to the best-fit relation (ϵ_\perp , the scatter unaccounted for by the observational uncertainties and therefore assumed to be intrinsic to the relations), and including uncertainties in both variables. We use flat priors for a , and b , and $\epsilon_\perp \geq 0$ for ϵ_\perp . The best-fitting relations are shown in Fig. 2, and the best-fitting coefficients are listed in Table 1, where we also quote the observed vertical RMS scatter of the relations (σ_{M_*} and σ_{j_*}). We emphasise that σ_{M_*} and σ_{j_*} measure the scatter of the data, but do not weight the observational errors, while ϵ_\perp does, and it is assumed to be inherent to the scaling laws.

The literature on the TFR and FR at $z \sim 1$ is extensive, as recently summarised in [Sharma et al. \(2024\)](#) and [Espejo Salcedo et al. \(2025\)](#). Formally, the slope of our TFR is higher than the value of $a = 3.03$ by [Sharma et al. \(2024\)](#) and similar to those ($a \sim 3.6 - 3.8$) reported by [Di Teodoro et al. \(2016\)](#); [Harrison et al. \(2017\)](#); [Übler et al. \(2017\)](#); [Pelliccia et al. \(2019\)](#); [Tiley et al. \(2019\)](#); [Abril-Melgarejo et al. \(2021\)](#), although it should be kept in mind the usage of different velocity conventions when defining the TFR, as well as the fact that some of the above studies fixed the slope to the local value from [Reyes et al. \(2011\)](#). Our FR slope is slightly below the $a \sim 0.5 - 0.6$ reported by [Harrison et al. \(2017\)](#); [Gillman et al. \(2020\)](#) and [Bouché et al. \(2021\)](#), but entirely consistent within the uncertainties. Comparing the intercepts is more challenging since different studies employ different pivot points; however, visual inspection suggests a fair agreement within $\sim 10 - 20\%$. The level of agreement between the various studies is encouraging, although somewhat surprising given the differing analyses among them. Given our thorough methodology (kinematic modelling and beam smearing corrections are more robustly determined, NIR JWST data are considered for SED fitting and surface brightness profiles, and realistic AD corrections are incorporated), we expect our best-fitting parameters to be as accurate as possible, considering the quality of the currently available data.

Table 1: Best-fitting coefficients (a, b, ϵ_\perp) and vertical RMS scatter (σ_{M_*} for the TFR and σ_{j_*} for the FR) of our $z = 0.9$ TFR and FR.

Scaling law	a	b	ϵ_\perp	σ_{M_*} or σ_{j_*}
$M_* - V_{\text{circ,f}}$	$3.82^{+0.55}_{-0.40}$	$10.27^{+0.06}_{-0.07}$	$0.06^{+0.01}_{-0.01}$	0.26
$j_* - M_*$	$0.44^{+0.06}_{-0.06}$	$2.86^{+0.02}_{-0.02}$	$0.11^{+0.02}_{-0.01}$	0.13

4.2. Evolution since the Universe's half-age

Here we explore whether the scaling relations have evolved since $z \sim 1$. Among the many low- z measurements, we adopt [Marasco et al. \(2025\)](#) as our $z = 0$ reference for three main reasons: 1) their analysis is based on the SPARC sample ([Lelli et al. 2016](#)), which we used to calibrate our methods (Appendix B);

2) their M_* estimates are based on the same technique as ours; and 3) they adopt the same pivot values in their fitting ($10^{10.5} M_\odot$ and 150 km/s), which simplifies the comparison. We note that [Marasco et al. \(2025\)](#) used directly H I kinematics to estimate $V_{\text{circ,f}}$ and j_* without applying AD corrections, but we do not expect this to introduce big differences since rotation-to-dispersion ratios of H I data in the nearby Universe are much larger than those of our sample, leading to small differences between $V_{\text{H}\text{I}}$, $V_{\text{circ,f}}$, and V_* , specially at $M_* > 10^8 M_\odot$ ([Mancera Piña et al. 2021a](#)). [Marasco et al. \(2025\)](#) reports a slope $a = 5.21 \pm 0.18$, intercept $b = 10.16 \pm 0.03$, intrinsic scatter $\epsilon_\perp = 0.039$, and vertical observed scatter $\sigma_{M_*} = 0.274$ for the local TFR, and $a = 0.52 \pm 0.03$, $b = 3.04 \pm 0.03$, $\epsilon_\perp = 0.128$, and $\sigma_{j_*} = 0.171$ for the local FR (similar to e.g. [Posti et al. 2018](#); [Mancera Piña et al. 2021a](#)).

As shown in Fig. 2, our TFR and FR at $z = 0.9$ differ from those at $z = 0$. The evolution of the relations can also be visualised in Fig. 3, where we compare the posterior distributions of our best-fitting parameters to those of [Marasco et al. \(2025\)](#). As seen from Fig. 3 (note that unaccounted uncertainties in masses and kinematics may further broaden the confidence levels), our results present moderate evidence for the evolution of the TFR, and strong evidence for the evolution of the FR. In both relations, the evolution is driven by changes in slopes and intercepts, rather than by the intrinsic scatter. Near $z \sim 1$, the TFR was shallower and had a higher intercept by about 0.1 dex. On the other hand, the FR had a slightly shallower slope (unlike the substantial changes reported by [Espejo Salcedo et al. 2025](#) at $z \approx 1.5 - 2.5$) and its intercept was lower by ~ 0.2 dex. This latter offset has also been found by theoretical studies based on disc-stability conditions ([Obreschkow et al. 2015](#)) and semi-analytical models ([Stevens et al. 2016](#)), as well as observational studies ([Harrison et al. 2017](#); [Swinbank et al. 2017](#)).

4.3. Caveats and systematics

Here, we discuss some caveats in our analysis and the potential for systematics to impact our results. First, we investigate the hypothetical case in which our observational uncertainties may have been somewhat underestimated (e.g. by our use of $z = 0$ calibrations to estimate $\sigma_{z,*}$, or the assumption of constant scale heights in Sect. 3; note that otherwise our uncertainties account for the various individual uncertainties that enter our derivation of $V_{\text{circ,f}}$ and j_*). Since underestimated errors can bias the recovery of the relations ([Übler et al. 2017](#); [Alcorn et al. 2018](#); [Espejo Salcedo et al. 2025](#)), we aim to estimate a realistic additional error budget for our observations to assess the robustness of our best-fitting parameters. A reasonable approach is to inflate the uncertainties in $\log(V_{\text{circ,f}})$ and $\log(j_*)$ by an amount so that the intrinsic perpendicular scatter (ϵ_\perp) in both scaling relations is nullified. This turns out to be 0.05 dex for the former and 0.1 dex for the latter. However, refitting the TFR and FR shows that such inflation has no repercussion on our results, since the best-fitting slopes and intercepts remain unchanged. Following [Übler et al. \(2017\)](#), we also explored by how much our uncertainties in $\log(M_*/M_\odot)$ would need to be underestimated to make the $z = 0.9$ TFR consistent with the local one from [Marasco et al. \(2025\)](#), finding that only a severe underestimation by 0.4 dex would do it, although this would also result in a stronger evolution of the FR (which would have decrease slope by 0.1).

Next, we investigate two additional questions: Could there be systematic effects that affect the observed evolution in our TFR and FR? Could our sample be missing a galaxy population that, when included, would weaken the evolution of the relations? We

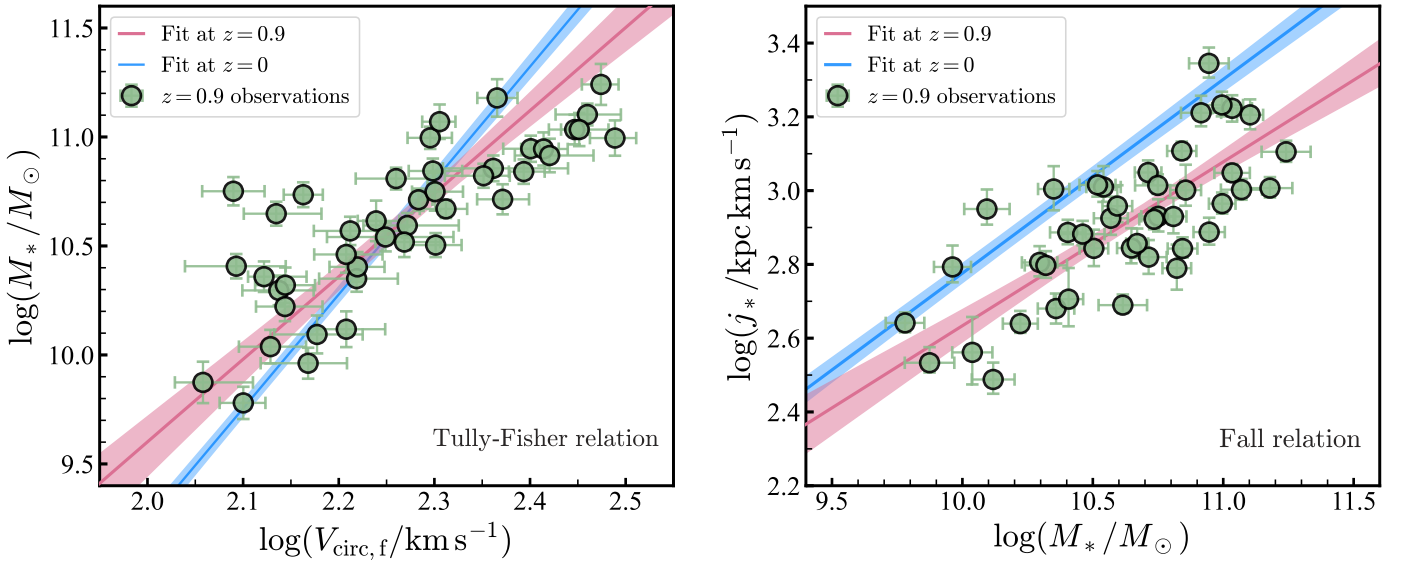


Fig. 2: Our $z = 0.9$ scaling laws. The TFR is shown on the *left*, and the FR on the *right*. Our measurements are shown with the green markers, while the best-fit relations and their 1σ confidence bands are shown as pink solid curves and bands, respectively. For comparison, we show the $z = 0$ TFR and FR from Marasco et al. (2025).

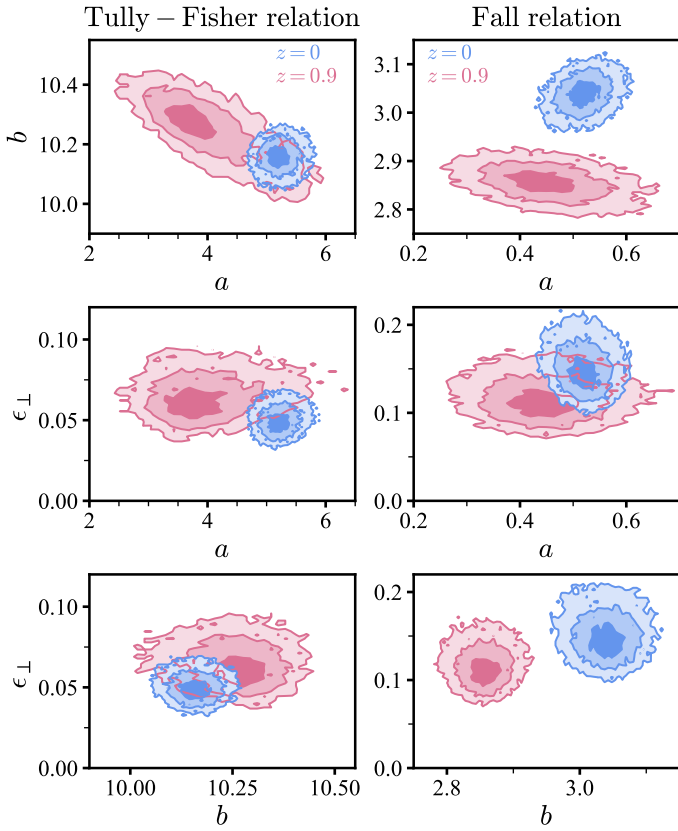


Fig. 3: Posterior distributions of the best-fitting TFR and FR. The distributions of low- and high- z disc galaxies are shown in blue (from Marasco et al. 2025) and pink (this work), respectively. The contours encompass the 0.393, 0.865, and 0.989 percentiles, corresponding to 1, 2, and 3σ in 2D distributions.

start with the first question. Considering the direction of the evolution in the TFR, we are particularly interested in a possible systematic error or bias that results in $V_{\text{circ},f}$ measurements progressively biased low for decreasing M_* , since this could cause

the shallower slope and higher intercept in the $z = 0.9$ TFR compared to the $z = 0$ TFR. We find it unlikely that this is the case. First, we point out that the typical effect of the AD correction is to increase the velocities of low-mass galaxies; therefore, ignoring it would amplify the difference rather than reducing it. In fact, without AD corrections, the TFR and FR would have changes of slopes and intercepts given by $\delta a = a - a_{\text{noADC}} = 0.5$ and $\delta b = b - b_{\text{noADC}} = -0.17$ dex for the TFR, and $\delta a = -0.05$ and $\delta b = 0.02$ dex for the FR. This highlights the importance of applying the AD corrections described in Sect. 3, which we encourage future studies to incorporate.

Next, we can examine if any factors within our calculation of $V_{\text{AD},*}$ could lead to underestimating $V_{\text{circ},f}$ for decreasing M_* . For this, we would need to have systematically underestimated $\sigma_{\text{H}\alpha}$ and/or overestimated $R_{\text{eff},\text{H}\alpha}$. A strong underestimation of $\sigma_{\text{H}\alpha}$ is unlikely: our kinematic software has been shown to recover gas velocity dispersions within 20% for data with spatial resolution and S/N like ours (Di Teodoro & Fraternali 2015), and an underestimation of 20% on $\sigma_{\text{H}\alpha}$ at our lowest rotational speeds (~ 120 km/s) leads to a $V_{\text{circ},f}$ higher by 10% at most (0.04 dex in $\log(V_{\text{circ},f})$). Our assumed $R_{\text{eff},\text{H}\alpha} = 1.13(\pm 0.05)R_{\text{eff},*}$ is well calibrated at $z = 1$ (Nelson et al. 2016; Wilman et al. 2020), and since $R_{\text{eff},\text{H}\alpha} > R_{\text{eff},*}$ is a condition for the well known inside-out growth of galaxy discs (Nelson et al. 2012, 2016), there is little room for an overestimation. Fixing $R_{\text{eff},\text{H}\alpha} = R_{\text{eff},*}$ plus a 20% underestimation of $\sigma_{\text{H}\alpha}$ would only lead to an increase in $\log(V_{\text{circ},f})$ of around 0.03, 0.02, 0.01, and 0.005 dex at $\log(M_*/M_\odot) = 10, 10.5, 11, 11.5$, which is largely insufficient to account for the evolution shown by the TFR (see also Sect. 4.2).

Two additional scenarios that could bias the slope of our TFR to shallower values are if we systematically overestimate M_* for low-luminosity galaxies and/or if we systematically overestimate disc inclinations at low M_* . We also deem these cases unlikely. On the one hand, our M_* recovery methods have been calibrated at $z = 0$, yielding excellent agreement with dynamical estimates and stellar population models (Marasco et al. 2025). On the other hand, our inclinations come from accurate modelling of the JWST and HST imaging of our galaxies (which we find to be in good agreement with H α morphology inclinations),

and, most importantly, show no correlation with the location of galaxies in the TFR and FR. We also note that in Sect. 2 we assumed the same intrinsic thickness $q_0 = 0.2$ for all galaxies when converting the observed axis ratios to inclinations, but if we had assumed thicker discs for lower-mass galaxies, their inclinations would be larger, leading to lower rotational speed, hence to a shallower TFR slope. So far, we have focused on our $z = 0.9$ TFR, but it is crucial to note that systematic corrections increasing the velocities at the low M_* end more than at the high M_* end would drive a more substantial evolution of the FR at $z = 0.9$, as it would become shallower.

We turn now our attention to the second question formulated above: Could we be missing a subset of the star-forming galaxy population that would change our TFR and FR and weaken their evolution? Given our imposed selection criteria, which require only resolved galaxies with clear velocity gradients, we may be missing the most compact and slowly rotating galaxies within our observed M_* range. However, by comparing our sample against the $z = 0.9$ stellar mass-size relation from Martorano et al. (2024) in Fig. 1, it becomes evident that although the scatter of our sample is not as wide as the full distribution from Martorano et al. (2024) and we may lack the rare smallest systems, we should not be missing a significant fraction of compact galaxies at any M_* . It is also important to note that if we were missing slowly-rotating or very compact galaxies at all masses, the intercepts of our TFR and FR would increase and decrease, respectively, driving a more substantial evolution than reported above. To weaken the evolution in our relations, we would need to be missing a significant population of fast-rotating galaxies at all masses below $\log(M_*/M_\odot) \lesssim 10.8$, which does not seem feasible, as there is no reason to expect such a population would go undetected.

Finally, we also acknowledge that if the TFR and FR at $z = 0$ and $z = 0.9$ have some curvature, the more limited M_* span of our sample (reaching $\log(M_*/M_\odot) > 9.5$) compared to the $z = 0$ samples (reaching $\log(M_*/M_\odot) \sim 7$, e.g. Marasco et al. 2025; Mancera Piña et al. 2025) could affect the best-fitting power-law parameters. For example, fitting the $z = 0$ data from Marasco et al. (2025) masking out all galaxies with $\log(M_*/M_\odot) < 9.5$ results in different local relations. On the one hand, the TFR with the cut in mass has a slope that is 0.74 lower and an intercept that is 0.09 dex higher. On the other hand, the FR cut with the mass cut has a slope that is 0.13 higher and an intercept that is 0.04 dex lower. Understanding precisely the actual effect on our $z = 0.9$ relations will only be possible with the next generation of IFUs to be installed at the ELT, and partially with upcoming ERIS data, which has the same spatial resolution as KMOS but better spectral resolution.

In summary, the potential systematic effects discussed above appear too small to significantly affect our TFR and FR (particularly if they are unbroken power laws). Unless additional, as yet unidentified, systematics are at play, our analysis suggests evolution in both relations.

5. Links with dark matter haloes' scaling relations

5.1. Drivers of the evolution

Next, we examine some simple consequences of our empirical findings in the context of the link between the scaling relations of disc galaxies and their dark matter haloes. We start with the virial relations for dark matter haloes in CDM-like cosmologies

(see Cimatti et al. 2019)

$$M_{\text{vir}} = \frac{1}{G H(z)} \sqrt{\frac{2}{\Delta_c(z)}} V_{\text{vir}}^3, \quad (9)$$

$$j_{\text{vir}} = \frac{2 \lambda}{H(z) \sqrt{\Delta_c(z)}} V_{\text{vir}}^2, \quad (10)$$

where G is the gravitational constant, $\Delta_c(z)$ the critical density for virialisation, $H(z)$ the Hubble parameter, and λ the Bullock et al. (2001) spin parameter which follows a log-normal distribution peaked at $\log \lambda \approx -1.456$, irrespective of z and M_{vir} (but see also Bett et al. 2007, Teklu et al. 2015, and Rodriguez-Gomez et al. 2017 for potential subtle dependencies on M_{vir} , z , and morphology). These equations⁶ can be rewritten in terms of the observables M_* , $V_{\text{circ,f}}$, and j_* , and the ratios $f_V = V_{\text{circ,f}}/V_{\text{vir}}$, $f_j = j_*/j_{\text{vir}}$, and $f_M = M_*/M_{\text{vir}}$, such that

$$M_* = \frac{\sqrt{2} (f_M/f_V^3)}{G H \sqrt{\Delta_c}} V_{\text{circ,f}}^3, \quad (11)$$

$$j_* = \frac{2 \lambda (f_j/f_V^2)}{H \sqrt{\Delta_c}} V_{\text{circ,f}}^2. \quad (12)$$

Evaluating these equations at redshift z and $z = 0$ we have

$$\frac{V_{\text{circ,f}}(M_*, z)}{V_{\text{circ,f}}(M_*, 0)} = \left[\frac{f_V(M_*, z)}{f_V(M_*, 0)} \right] \left[\frac{f_M(M_*, z)}{f_M(M_*, 0)} \right]^{-1/3} \left[\frac{\Delta_c(z)}{\Delta_c(0)} \right]^{1/6} \left[\frac{H(z)}{H(0)} \right]^{1/3}, \quad (13)$$

$$\frac{j_*(M_*, z)}{j_*(M_*, 0)} = \left[\frac{f_j(M_*, z)}{f_j(M_*, 0)} \right] \left[\frac{f_M(M_*, z)}{f_M(M_*, 0)} \right]^{-2/3} \left[\frac{\Delta_c(z)}{\Delta_c(0)} \right]^{-1/6} \left[\frac{H(z)}{H(0)} \right]^{-1/3}, \quad (14)$$

which give the z evolution of the TFR and FR.

We first test the hypothetical scenario in which the TFR and FR evolve exclusively through the redshift dependence of the H and Δ_c . In this case, f_M , f_j , and f_V are assumed to be independent of z (although may depend on M_*), and the first two terms on the right hand side of Eqs. 13 and 14 vanish. With these expressions under the cosmology-only halo scaling hypothesis, we can propagate the TFR and FR from Marasco et al. (2025) back to $z = 0.9$ and compare with our observed $z = 0.9$ relations. For our cosmology, we have $H(z = 0.9) = 116.3 \text{ km s}^{-1} \text{ Mpc}^{-1}$, $\Delta_c(z = 0) = 101$ and $\Delta_c(z = 0.9) = 154$ (Bryan & Norman 1998). The results of this exercise are shown in the top panels of Fig. 4. The evolved TFR and FR are even more discrepant with respect to the $z = 0.9$ relations than the observed laws at $z = 0$. Note also that the systematic offsets needed to match our data with the cosmology-only halo scaling hypothesis are significantly larger than those discussed in Sect. 4.3. Therefore, to match the data, $f_V f_M^{-1/3}$ and $f_j f_M^{-2/3}$ must evolve.

At this stage, it is instructive to rearrange Eqs. 11 and 12 as

$$f_M(M_*, z) = \sqrt{\frac{\Delta_c(z)}{2}} G H(z) M_* \left(\frac{f_V(M_*, z)}{V_{\text{circ,f}}(M_*, z)} \right)^3, \text{ and} \quad (15)$$

⁶ Eq. 10 is exact for haloes with singular isothermal sphere (SIS) profiles, and accurate within $\sim 10\%$ for NFW haloes (Navarro et al. 1997) with $10 < \log(M_{\text{vir}}/M_\odot) < 14$ (e.g. Bullock et al. 2001).

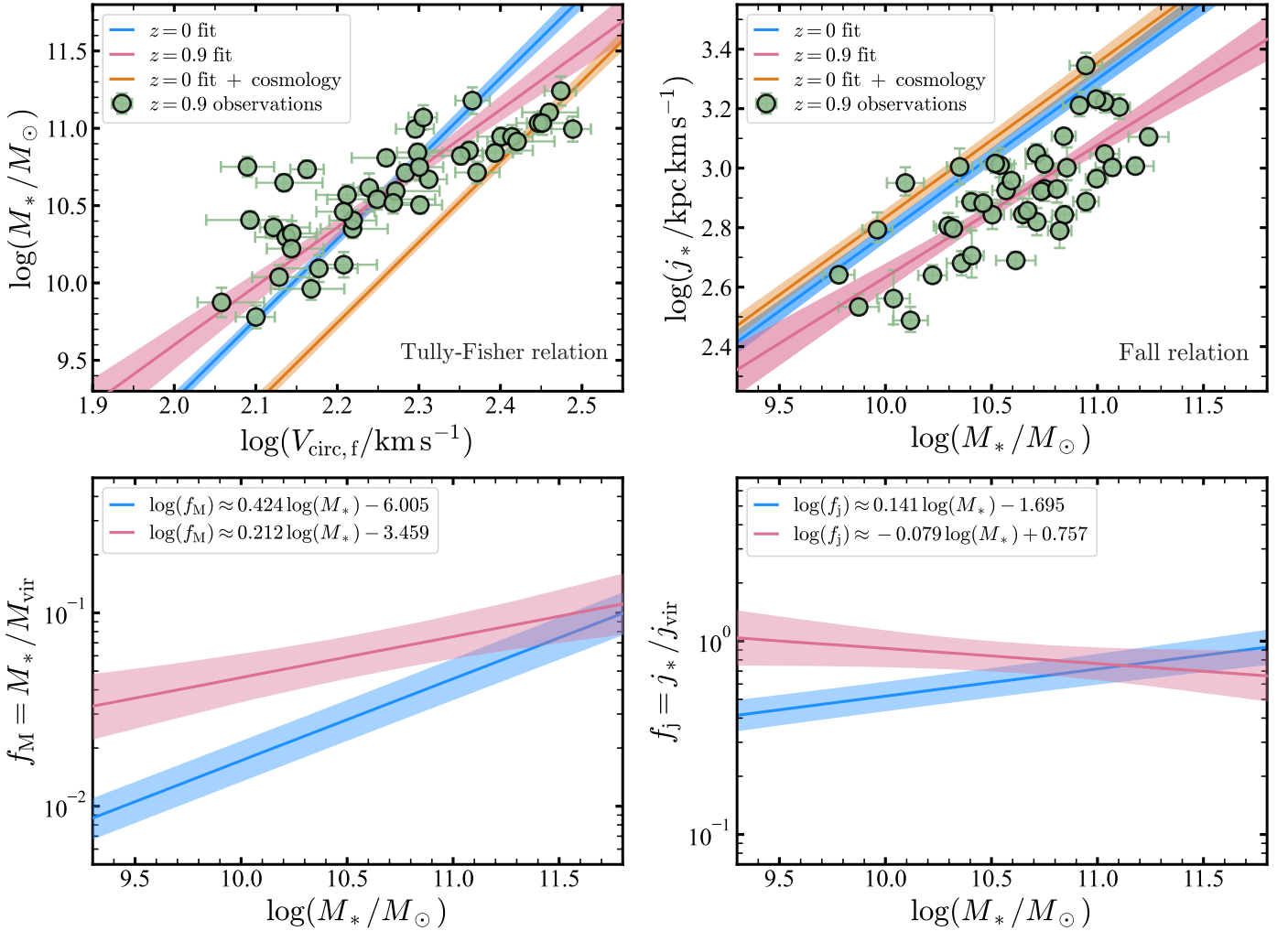


Fig. 4: Drivers of the evolution in our scaling relations. The *top* panels compare how the local TFR and FR (blue curves) would evolve (orange curves) if the only changes are the z evolution of the Hubble parameter and the density contrast, against our high- z data (green markers) and best fits (pink curves). The results imply an evolution of $f_V f_M^{-1/3}$ and $f_j f_M^{-2/3}$. The *bottom* panels show f_M at $z = 0$ (blue) and $z = 0.9$ (pink) as a function of M_* implied by our best-fitting relations, after assuming $f_V = 1.3 \pm 0.1$. In all the panels, bands correspond to 1σ confidence bands around the mean relations. Note that the vertical axis span in the bottom panels is the same, highlighting the stronger mass dependency of f_M over f_j .

$$f_j(M_*, z) = \frac{H(z) \sqrt{\Delta_c(z)}}{2\lambda} j_*(M_*, z) \left(\frac{f_V(M_*, z)}{V_{\text{circ},f}(M_*, z)} \right)^2. \quad (16)$$

From these equations, it is clear that f_M and f_j at any z are entirely specified by the cosmological redshift dependence of the Hubble parameter and density contrast, by f_V , and by the observed TFR and FR. The ratio f_V depends on the baryonic and dark matter expansion and contraction, but varies only weakly with M_* (see Dutton et al. 2010; McGaugh 2012). For instance, Reyes et al. (2012) combined kinematic and weak-lensing observations and found $f_V \approx 1.3 - 1.4$ for galaxies with $9.8 < \log(M_*/M_\odot) < 10.8$ at $z = 0$. In addition, results from Posti et al. (2019a) and Mancera Piña et al. (2025) on mass models from rotation curve decomposition imply in $f_V \approx 1.2 - 1.4$ for galaxies with $100 < V_{\text{circ},f}/\text{km s}^{-1} < 350$. Based on this, and for simplicity, we neglect any M_* dependency and consider $f_V = 1.3$ with a 1σ scatter of 0.1. We further assume that f_V does not change with z ; although no observational constraints exist, ide-

alised models suggest that f_V evolves significantly only at $z \gtrsim 2$ (Somerville et al. 2008; Dutton et al. 2011).

From the best-fit TFR and FR form this work and Marasco et al. (2025), we compute the resulting ratios, shown in the bottom panels of Fig. 4. Solid lines show the median relations, and the confidence bands the 16th-84th percentile range, derived from the sampling of the best-fitting TFR and FR (including their intrinsic scatter ϵ_\perp). For the $f_M - M_*$ and $f_j - M_*$ relations at $z = 0$, the width is around 0.08–0.1 dex. For the $z = 0.9$ relations, the width is around 0.10–0.13 dex, respectively. For completeness, we also carry out the exercise of propagating the observed vertical scatter in the TFR (σ_{M_*}) and FR (σ_{j_*}) into the $f_M - M_*$ and $f_j - M_*$ relations. At $z = 0$, σ_{M_*} (σ_{j_*}) propagates into a scatter of 0.16 (0.20) dex at fixed M_* (slightly smaller but comparable to literature values, e.g. Romeo et al. 2020, 2023). At $z = 0.9$, σ_{M_*} (σ_{j_*}) propagates into a scatter of 0.20 (0.19) dex at fixed M_* . Overall, our redshift comparison reveals changes in f_M and f_j from $z = 0.9$ to the present, which we discuss next.

5.2. The evolution of f_M

The bottom left panel of Fig. 4 shows f_M at $z = 0$, exhibiting the same single power-law behaviour found for nearby star-forming galaxies based on rotation curve decomposition (e.g. Posti et al. 2019a; Di Teodoro et al. 2023; Mancera Piña et al. 2025). In particular, f_M at $z = 0$ is well described by the expression $\log(f_M) = 0.424 \log(M_*/M_\odot) - 6.002$. On the other hand, at $z = 0.9$ we find higher f_M values for $M_* < 10^{12} M_\odot$ and, crucially, a weaker M_* dependency driven by the shallower TFR at $z = 0.9$, with $\log(f_M) = 0.212 \log(M_*/M_\odot) - 3.459$.

To place the observed scaling relations in the broader context of halo and galaxy assembly, we can explore the basic assumption that main-sequence star-forming galaxies at $z = 1$ are the progenitors of the main-sequence star-forming population at $z = 0$. To show this schematically, in the top panel of Fig. 5 we construct a simple toy model in which the local $f_M - M_*$ relation (blue curve) is populated with mock galaxies (blue circles) and evolved backwards in time to $z = 0.9$ (squares). The bottom panel recasts the same comparison into the more familiar stellar-to-halo mass plane, highlighting the relative individual growth of M_* and M_{vir} . For this, we assume that the galaxies' stellar mass evolves following the main sequence SFR – M_* – z relation of Leja et al. (2022), and that their halo growth follows the formalism by van den Bosch et al. (2014). This exercise yields a steeper relation at $z = 0.9$ (pink squares), which departs from our measurements (pink curve). Notably, this unveils an apparent discrepancy between our observational results and standard framework of galaxy mass assembly. This can be seen clearly by drawing arbitrary evolutionary tracks from the $z = 0.9$ to the $z = 0$ relations in the bottom panel of Fig. 5, under the simple requirement that stellar masses do not decrease with time. In this picture, massive haloes must already be largely assembled by $z = 0.9$, while low-mass systems continue building a substantial fraction of their halo mass at later times⁷. This differs from the established theoretical halo growth, in which massive haloes exhibit stronger fractional growth at late times than their lower-mass counterparts (e.g. Fakhouri et al. 2010; van den Bosch et al. 2014; Correa et al. 2015).

While the above toy model is an oversimplification of the complex processes in the evolution of individual galaxies, it suggests an inconsistency between our results and standard halo mass growth formalisms. We have performed preliminary explorations of hydrodynamical simulations (specifically TNG100, Nelson et al. 2019) to shed light on this, but we find significant differences between catalogue parameters and our measurements to carry out a meaningful comparison, and we plan to do so in the future.

We also consider additional factors that could potentially bias our results and alleviate the potential halo growth discrepancy. As shown in the top-left panel of Fig. 4, reconciling the $z = 0.9$ TFR with the cosmology-only halo scaling hypothesis would that the circular speeds of galaxies with $\log(M_*/M_\odot) \lesssim 10.7$ have been underestimated by $\sim 50\%$. As discussed extensively in Sect. 4.3, the uncertainties considered in this work are insufficient to account for this discrepancy on their own. Another possibility is to consider that unknown additional systematic effects or inappropriate assumptions may bias our results.

⁷ We note that sensible variations in f_V cannot explain the discrepancy. For example, reducing f_V by 10 – 20% (e.g. Dutton et al. 2011) leaves the slope unchanged and does not move the $z = 0.9$ relation below that at $z = 0$. Matching the data would require an implausibly strong mass dependence of f_V (Posti et al. 2019a; Mancera Piña et al. 2025) and $f_V < 1$ for $V_{\text{circ},f} < 250 \text{ km s}^{-1}$, which is unphysical (McGaugh 2012).

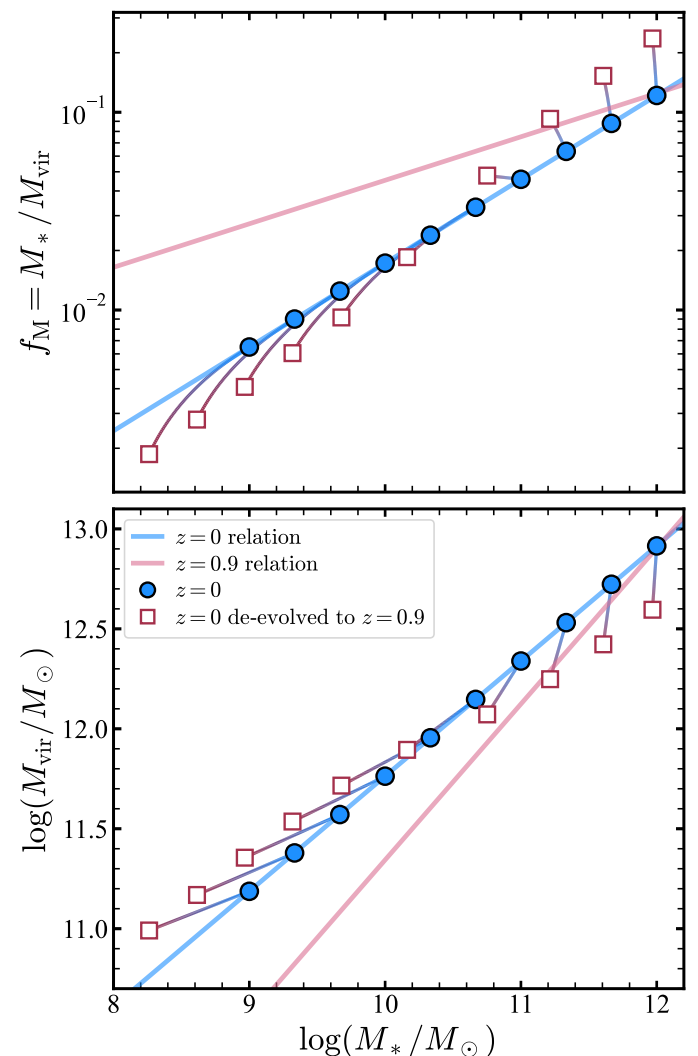


Fig. 5: Comparison between our inferred $f_M - M_*$ (top) and $M_{\text{vir}} - M_*$ (bottom) relations and an idealised toy model of mass assembly. The model considers a population of galaxies (blue circles) lying in the $z = 0$ relations (blue curves), which are then traced back to $z = 0.9$ (squares) assuming theoretical stellar and halo mass growths. Galaxy downsizing and halo growth histories yield $z = 0.9$ relations (squares) with slopes different from those observed at $z = 0$ (pink solid curve). The only way to reconcile the stellar mass growth of galaxies with our inferred relations at $z = 0.9$ is if low-mass haloes grew more than high-mass haloes since $z = 0.9$, unlike CDM expectations. This likely indicates that the galaxies populating our $z = 0.9$ relations do not evolve into those that conform to the relations at $z = 0$.

Crucially, we note that such effects must have also been present in previous TFR determinations at $z \sim 1$, which report slopes consistent with ours (see Sect. 4.1). Alternatively, one may be inclined to conclude that ionised gas kinematics cannot be used to infer dynamical properties of high- z star-forming galaxies, regardless of a careful approach like ours, which includes robust 3D kinematic modelling, AD corrections, Sérsic modelling of NIR data, and homogeneous stellar mass determinations.

An additional factor to consider is that the galaxies used to establish the $z = 0$ relations are not necessarily the descendants of the observed $z \sim 1$ population (i.e. a case of progenitor bias; e.g., van Dokkum & Franx 1996, 2001). In this case, the

changes in the scaling relations may partly reflect differences in the sampled progenitors and descendants rather than the typical evolution of individual galaxies. For instance, the most massive galaxies in our sample (which also show the clearer systematic deviation from the $z = 0$ TFR) are likely to have quenched and undergone morphological transformations by $z = 0$. This should be further explored through simulations tracking the evolution of individual galaxies, but the careful work required is beyond our current scope. We note that potential progenitor bias and similar selection effects are also present in other high- z analyses, and mitigating this bias will require tracing the TFR and FR across finer redshift intervals and to earlier epochs. Upcoming facilities such as SKA, ALMA, Euclid, and Roman will also provide direct constraints on galaxy kinematics and halo properties through deep cold-gas observations and weak-lensing measurements, and will be key to obtaining a more definitive picture.

Finally, we would like to highlight the recent studies based on abundance matching and angular clustering by [Shuntov et al. \(2025\)](#) and [Paquereau et al. \(2025\)](#), respectively. Looking at the COSMOS field with JWST, the above authors also find tentative evidence for higher values of f_M at $z \sim 1$ than at $z \sim 0$, although without an explanation yet. This is unlike previous abundance-matching studies⁸, which typically suggest a higher f_M at $z = 0$ than at $z = 1$, with only mild evolution in slope ([Moster et al. 2010](#)). State-of-the-art hydrodynamical simulations generally show little redshift evolution in f_M ([Chaikin et al. 2025](#)), so clearly obtaining additional observational constraints will be key to understanding the apparent discrepancy highlighted above.

5.3. The evolution of f_j and f_R

Next, we turn our attention to f_j , shown in the bottom right panel of Fig. 4. At both redshifts, f_j depends more weakly on M_* than f_M (see also e.g. [Posti et al. 2019b](#); [Di Teodoro et al. 2023](#); [Romeo et al. 2023](#)). Within $9.5 < \log(M_*/M_\odot) < 11.5$, f_M at $z = 0$ increases by a factor of ~ 2 , while at $z = 0.9$ it decreases by 30%. This implies that while f_j increases with M_* at $z = 0$, it decreases at $z = 0.9$. The $f_j - M_*$ relations⁹ are well described by the power laws $\log(f_j) = 0.141 \log(M_*/M_\odot) - 1.695$ at $z = 0$, and $\log(f_j) = -0.079 \log(M_*/M_\odot) + 0.757$ at $z = 0.9$. Our results also indicate that disc galaxies with $\log(M_*/M_\odot) \lesssim 11.1$ have lowered their f_j over the last ~ 8 Gyr, and more massive galaxies have raised it.

Different mechanisms can increase or decrease f_j such as outflows, galactic fountains, stripping, minor and major mergers, and dynamical friction (e.g. [van den Bosch et al. 2001](#); [Brook et al. 2012](#); [Romanowsky & Fall 2012](#); [Lagos et al. 2017](#); [Irodotou et al. 2019](#)). Following the reasoning presented in [Romanowsky & Fall \(2012\)](#) and [Lagos et al. \(2018\)](#), we speculate that feedback-driven outflows or mergers (or a combination of both) could explain our observational results. In the case of outflows, they could be driven by stellar feedback, given the high star formation rates at $z = 0.9$. Since most outflows likely originate from regions with high star formation efficiencies

near galaxy centres, feedback preferentially removes low- j_* material (e.g. [Brook et al. 2011](#)), effectively raising f_j at $z = 0.9$ compared to $z = 0$ in the mass regime in which stellar feedback is efficient. In the case of mergers, our results would suggest that galaxies with $\log(M_*/M_\odot) \lesssim 11.1$ at $z = 0.9$ further experience dry mergers, leading to a decrease in f_j by $z = 0$.

Our results also have immediate implications for the relative sizes of galaxy discs compared to their host haloes. For exponential discs (a good approximation for our sample; see Fig. 1) embedded in SIS haloes, one obtains $f_R = R_{\text{eff},*}/R_{\text{vir}} = (1.678/\sqrt{2}) \lambda f_j/f_V$ (e.g. [Fall & Efstathiou 1980](#); [Fall 1983](#); see also [Mo et al. 1998](#) for the NFW case). For $f_V = 1.3$, this reduces to $f_R \approx 0.032 f_j$, so that the evolution of $f_R(M_*, z)$ is fully specified by that of $f_j(M_*, z)$ in Fig. 4. Our finding of only weak variation in $f_R(M_*, z)$ agrees well with previous semi-empirical studies (e.g. combining observed galaxy sizes with abundance-matching halo sizes; [Huang et al. 2017](#); [Somerville et al. 2018](#)) and with results from hydrodynamical simulations ([Grand et al. 2017](#); [Rodriguez-Gomez et al. 2022](#); [Somerville et al. 2025](#)).

5.4. A short remark on gas content

An important aspect to keep in mind is that throughout this study, we have only considered the stellar component of f_M and f_j , since resolved cold gas measurements at $z \sim 1$ remain scarce, partly due to gaps between ALMA bands. Yet, at $z = 0$ it is well established that cold gas carries a substantial fraction of the angular momentum budget and contributes significantly to the baryonic j of galaxies, except in the most massive discs (e.g. [Mancera Piña et al. 2021a,b](#); [Romeo et al. 2023](#)). Moreover, the baryon-to-halo mass relation is shallower than the stellar one at $z = 0$ ([Romeo et al. 2023](#); [Mancera Piña et al. 2025](#)), and the higher cold gas fractions at earlier epochs ([Tacconi et al. 2020](#)) make this even more relevant at $z \sim 1$.

We note here that including the cold gas component would likely strengthen the apparent discrepancy with downsizing highlighted in Fig. 5, since galaxies at $z = 0.9$ will grow more in baryonic mass than galaxies at $z = 0$. At the same time, cold gas kinematics would help reduce the observational uncertainties in our analysis (see Sect. 3), enabling a more robust reassessment of the evolution of the baryon-to-halo mass and angular momentum ratios. Evidently, incorporating the cold gas reservoir is crucial for an integral picture of the evolution of f_M and f_j .

Beyond the cold gas in discs, a complete understanding of the drivers of f_M and f_j also requires accounting for the circumgalactic medium and large-scale cold gas, both of which exchange angular momentum with galaxies. Recent studies have explored this using advanced models and simulations (e.g. [Pezzulli et al. 2017](#); [Wang et al. 2022](#); [Afruni et al. 2023](#); [Liu et al. 2025](#); [Simons et al. 2025](#); [Wang et al. 2025](#)), but connecting these predictions to observations remains a key challenge for the years to come.

6. Summary and conclusions

In this work, we build the Tully-Fisher ($M_* - V_{\text{circ},f}$, TFR) and Fall ($j_* - M_*$, FR) relations for a sample of disc galaxies at $z = 0.9$. To do so, we first compile galaxies with public IFU H α kinematic data and space-based (JWST and HST) imaging. We apply different quality cuts, resulting in a high-quality sample of 43 star-forming rotationally supported discs (Fig. 1) with $5 \times 10^9 < M_*/M_\odot < 2 \times 10^{11}$ and $0.78 < z < 1.03$, encompassing

⁸ In Appendix C, we show the TFR required to match the f_M from abundance matching from [Moster et al. \(2010\)](#). Note that abundance matching also appears to be in tension with f_M measurements at $z = 0$ derived from rotation curves ([Posti et al. 2019a](#); [Di Teodoro et al. 2023](#); [Mancera Piña et al. 2025](#)).

⁹ Our estimate of f_j at $z = 0$ is compatible with previous estimates (e.g. [Fall & Romanowsky 2018](#); [Posti et al. 2019b](#); [Di Teodoro et al. 2023](#)) in its overall level, but not necessarily in the sign of the mass dependency.

a cosmic time when the Universe was half its current age. The galaxies in our sample are representative in terms of star formation rates, Sérsic indices, and effective radii for M_* and z ranges.

We derive robust kinematic models (Fig. A.1) that enable us to retrieve the intrinsic kinematics of the galaxies, despite the low spatial resolution, thereby improving upon previous literature. To account for the pressure-supported motions in our galaxies, we compute realistic asymmetric drift corrections, which allow us to convert our measured $H\alpha$ rotational velocities into circular speeds (whose flat value $V_{\text{circ},f}$ enters the TFR) and stellar rotational velocities (V_* , which is needed to compute j_* for the FR).

Paired with spatial and spectral modelling of JWST and HST data, we measure M_* , j_* , and $V_{\text{circ},f}$ (in a consistent way as done at $z = 0$), and we determine the $z = 0.9$ TFR and FR (Fig. 2, see also Fig. A.3). We parametrise the observed trends with power-laws (Fig. 2 and Table 1). We note that the asymmetric drift corrections have a non-negligible impact on the best-fitting TFR and FR, highlighting the importance of applying them.

By comparing our best-fitting relations with a recent determination in the nearby Universe based on cold neutral atomic gas, we detect moderate evolution of the TFR and a stronger evolution of the FR (Fig. 3). At $z = 0.9$, the TFR had a shallower mass dependency and a higher intercept. On the other hand, the FR had a slightly shallower slope and an intercept lower by about 0.2 dex. We discuss in detail different caveats that could affect the determination of our relations, finding that our results are robust against the presence of potential known systematics (but see below), unless the TFR and FR are intrinsically unbroken power laws.

A key aspect of this study is that we connect the observed TFR and FR with scaling relations for dark matter haloes. We find that the evolution of the relations cannot be explained by a model where the $z = 0$ TFR and FR are evolved to $z = 0.9$ by accounting for the z evolution of the Hubble parameter and density contrast alone (Fig. 4, top panels), but instead requires intrinsic variations in the galaxy mass and angular momentum assembly histories. Specifically, the quantities $f_V f_M^{-1/3}$ and $f_j f_M^{-2/3}$ must evolve with z , with $f_V = V_{\text{circ},f}/V_{\text{vir}}$, $f_M = M_*/M_{\text{vir}}$, and $f_j = j_*/j_{\text{vir}}$. Choosing a realistic f_V , we show the dependencies that f_M and f_j should have as a function of M_* and z given our TFR and FR (Fig. 4, bottom panels). This represents a significant improvement in the literature studying the f_M and f_j ratios, which often assume abundance-matching values rather than deriving them directly from the data. At $z = 0$, we find that both f_M and f_j increase with stellar mass, in agreement with previous observations.

Interpreting our evolving scaling relations with a simplified closed-box toy model of the evolution of individual galaxies results in a halo mass growth that appears to be in apparent discrepancy with the CDM hierarchical assembly of dark matter halos predicted (Fig. 5). To the best of our knowledge, this possible contradiction is reported here for the very first time. The problem must have been present in samples analysed in previous studies, but it emerges more clearly now thanks to our methodology of directly linking our observed scaling relations with those of dark matter haloes. The origin of this discrepancy in halo mass assembly is still to be fully understood, but we argue that plausible explanations include a progenitor bias effect, large unknown systematics, dramatically inaccurate assumptions in our and previous analyses, and/or questioning the reliability of ionised gas kinematics as a dynamical tracer.

As for f_j , it varies weakly with M_* at both $z = 0$ and $z = 0.9$ (Fig. 4). We find that across most of our mass regime,

the normalisation of f_j is slightly higher at $z = 0.9$. We speculate that this could be due to stellar feedback-driven outflows or a noticeable number of dry mergers after $z = 0.9$. The evolution of f_j also determines the evolution of the ratio $f_R = R_{\text{eff},*}/R_{\text{vir}} \approx 0.032 f_j$. Accordingly, we find relatively little evolution on $f_R(M_*, z)$, in agreement with previous theoretical and semi-empirical determinations.

Besides an improvement in the quality of kinematic data, the study of the time evolution of f_M and f_j needs to be complemented with models and simulations that incorporate the complexity of galaxy evolution in a cosmological context (e.g. Sales et al. 2009; Dutton & van den Bosch 2012; Pedrosa & Tissera 2015; Teklu et al. 2015; Lagos et al. 2017; El-Badry et al. 2018; Yang et al. 2024). Our observational results serve as vital benchmarks for such theoretical models.

Acknowledgements. We thank the referee for their helpful comments. We thank Joop Schaye, Filippo Fraternali, Francesca Rizzo, Pieter van Dokkum, and Marjijn Franx for valuable discussions. We also thank Christopher Harrison and Mark Swinbank for their clarifications on the KROSS data, Arjen van der Wel for his assistance on Sérsic models, and Henk Hoekstra for clarifications on weak-lensing estimates. PEMP is funded by the Dutch Research Council (NWO) through the Veni grant VI.Veni.222.364. EDT was supported by the European Research Council (ERC) under grant agreement no. 101040751. We have used the services from SIMBAD, NED, and ADS extensively, as well as the tool TOPCAT (Taylor 2005) and the Python packages NumPy (Oliphant 2007), Matplotlib (Hunter 2007), SciPy (Virtanen et al. 2020), and Astropy (Astropy Collaboration et al. 2018), for which we are thankful.

References

Abrial-Melgarejo, V., Epinat, B., Mercier, W., et al. 2021, A&A, 647, A152
 Afruni, A., Pezzulli, G., Fraternali, F., & Grønnow, A. 2023, MNRAS, 524, 2351
 Alcorn, L. Y., Tran, K.-V., Glazebrook, K., et al. 2018, ApJ, 858, 47
 Astropy Collaboration, Price-Whelan, A. M., Sipőcz, B. M., et al. 2018, AJ, 156, 123
 Bell, E. F. & de Jong, R. S. 2001, ApJ, 550, 212
 Bett, P., Eke, V., Frenk, C. S., et al. 2007, MNRAS, 376, 215
 Binney, J. 1977, ApJ, 215, 483
 Binney, J. & Tremaine, S. 2008, Galactic Dynamics: Second Edition
 Blumenthal, G. R., Faber, S. M., Primack, J. R., & Rees, M. J. 1984, Nature, 311, 517
 Bouché, N. F., Genel, S., Pellissier, A., et al. 2021, A&A, 654, A49
 Brook, C. B., Governato, F., Roškar, R., et al. 2011, MNRAS, 415, 1051
 Brook, C. B., Stinson, G., Gibson, B. K., et al. 2012, MNRAS, 419, 771
 Bryan, G. L. & Norman, M. L. 1998, ApJ, 495, 80
 Bullock, J. S., Dekel, A., Kolatt, T. S., et al. 2001, ApJ, 555, 240
 Burkert, A., Förster Schreiber, N. M., Genzel, R., et al. 2016, ApJ, 826, 214
 Carnall, A. C., McLure, R. J., Dunlop, J. S., & Davé, R. 2018, MNRAS, 480, 4379
 Casey, C. M., Kartaltepe, J. S., Drakos, N. E., et al. 2023, ApJ, 954, 31
 Catinella, B., Cortese, L., Tiley, A. L., et al. 2023, MNRAS, 519, 1098
 Chaikin, E., Schaye, J., Schaller, M., et al. 2025, arXiv e-prints, arXiv:2509.07960
 Charlot, S. & Fall, S. M. 2000, ApJ, 539, 718
 Cimatti, A., Fraternali, F., & Nipoti, C. 2019, Introduction to Galaxy Formation and Evolution: From Primordial Gas to Present-Day Galaxies (Cambridge University Press)
 Conselice, C. J., Bundy, K., Ellis, R. S., et al. 2005, ApJ, 628, 160
 Contini, T., Epinat, B., Bouché, N., et al. 2016, A&A, 591, A49
 Correa, C. A., Wyithe, J. S. B., Schaye, J., & Duffy, A. R. 2015, MNRAS, 452, 1217
 Cortese, L., Fogarty, L. M. R., Bekki, K., et al. 2016, MNRAS, 463, 170
 Courteau, S., Dutton, A. A., van den Bosch, F. C., et al. 2007, ApJ, 671, 203
 Cresci, G., Hicks, E. K. S., Genzel, R., et al. 2009, ApJ, 697, 115
 Dalcanton, J. J., Spergel, D. N., & Summers, F. J. 1997, ApJ, 482, 659
 de Araujo-Carvalho, A. E., Gonçalves, T. S., Krajnović, D., Menéndez-Delmestre, K., & de Isidó, N. 2025, arXiv e-prints, arXiv:2507.10544
 Di Teodoro, E. M. & Fraternali, F. 2015, MNRAS, 451, 3021
 Di Teodoro, E. M., Fraternali, F., & Miller, S. H. 2016, A&A, 594, A77
 Di Teodoro, E. M. & Peek, J. E. G. 2021, ApJ, 923, 220
 Di Teodoro, E. M., Posti, L., Fall, S. M., et al. 2023, MNRAS, 518, 6340

Di Teodoro, E. M., Posti, L., Ogle, P. M., Fall, S. M., & Jarrett, T. 2021, MNRAS, 507, 5820

Dunlop, J. S., Abraham, R. G., Ashby, M. L. N., et al. 2021, PRIMER: Public Release IMaging for Extragalactic Research, JWST Proposal. Cycle 1, ID. #1837

Dutton, A. A., Conroy, C., van den Bosch, F. C., Prada, F., & More, S. 2010, MNRAS, 407, 2

Dutton, A. A. & van den Bosch, F. C. 2012, MNRAS, 421, 608

Dutton, A. A., van den Bosch, F. C., Faber, S. M., et al. 2011, MNRAS, 410, 1660

Eisenstein, D. J., Willott, C., Alberts, S., et al. 2023, arXiv e-prints, arXiv:2306.02465

Ejdetjärn, T., Agertz, O., Östlin, G., Renaud, F., & Romeo, A. B. 2022, MNRAS, 514, 480

El-Badry, K., Quataert, E., Wetzel, A., et al. 2018, MNRAS, 473, 1930

Eldridge, J. J. & Stanway, E. R. 2009, MNRAS, 400, 1019

Espejo Salcedo, J. M., Glazebrook, K., Fisher, D. B., et al. 2025, MNRAS, 536, 1188

Fakhouri, O., Ma, C.-P., & Boylan-Kolchin, M. 2010, MNRAS, 406, 2267

Fall, S. M. 1983, in IAU Symposium, Vol. 100, Internal Kinematics and Dynamics of Galaxies, ed. E. Athanassoula, 391–398

Fall, S. M. & Efstathiou, G. 1980, MNRAS, 193, 189

Fall, S. M. & Romanowsky, A. J. 2018, ApJ, 868, 133

Forbes, D. A. & Gannon, J. 2024, MNRAS, 528, 608

Fouque, P., Bottinelli, L., Gouguenheim, L., & Paturel, G. 1990, ApJ, 349, 1

Fraternali, F., Karim, A., Magnelli, B., et al. 2021, A&A, 647, A194

Geesink, N. N., Mancera Piña, P. E., Lagos, C. d. P., & Kriek, M. 2025, A&A, 697, A87

Gillman, S., Swinbank, A. M., Tiley, A. L., et al. 2019, MNRAS, 486, 175

Gillman, S., Tiley, A. L., Swinbank, A. M., et al. 2020, MNRAS, 492, 1492

Girard, M., Fisher, D. B., Bolatto, A. D., et al. 2021, ApJ, 909, 12

Grand, R. J. J., Gómez, F. A., Marinacci, F., et al. 2017, MNRAS, 467, 179

Grogan, N. A., Kocevski, D. D., Faber, S. M., et al. 2011, ApJS, 197, 35

Hardwick, J. A., Cortese, L., Obreschkow, D., Catinella, B., & Cook, R. H. W. 2022, MNRAS, 509, 3751

Harrison, C. M., Johnson, H. L., Swinbank, A. M., et al. 2017, MNRAS, 467, 1965

Huang, K.-H., Fall, S. M., Ferguson, H. C., et al. 2017, ApJ, 838, 6

Hubble, E. P. 1926, ApJ, 64, 321

Hunter, J. D. 2007, Computing in Science & Engineering, 9, 90

Irodotou, D., Thomas, P. A., Henriques, B. M., Sargent, M. T., & Hislop, J. M. 2019, MNRAS, 489, 3609

Koekemoer, A. M., Aussel, H., Calzetti, D., et al. 2007, ApJS, 172, 196

Koekemoer, A. M., Faber, S. M., Ferguson, H. C., et al. 2011, ApJS, 197, 36

Kroupa, P. 2002, Science, 295, 82

Lagos, C. d. P., Stevens, A. R. H., Bower, R. G., et al. 2018, MNRAS, 473, 4956

Lagos, C. d. P., Theuns, T., Stevens, A. R. H., et al. 2017, MNRAS, 464, 3850

Leja, J., Speagle, J. S., Ting, Y.-S., et al. 2022, ApJ, 936, 165

Lelli, F., McGaugh, S. S., & Schombert, J. M. 2016, AJ, 152, 157

Levy, R. C., Bolatto, A. D., Teuben, P., et al. 2018, ApJ, 860, 92

Liu, K., Guo, H., Wang, S., et al. 2025, A&A, 693, A48

Mancera Piña, P. E., Fraternali, F., Oman, K. A., et al. 2020, MNRAS, 495, 3636

Mancera Piña, P. E., Fraternali, F., Oosterloo, T., et al. 2022, MNRAS, 514, 3329

Mancera Piña, P. E., Golini, G., Trujillo, I., & Montes, M. 2024, A&A, 689, A344

Mancera Piña, P. E., Posti, L., Fraternali, F., Adams, E. A. K., & Oosterloo, T. 2021a, A&A, 647, A76

Mancera Piña, P. E., Posti, L., Pezzulli, G., et al. 2021b, A&A, 651, L15

Mancera Piña, P. E., Read, J. I., Kim, S., et al. 2025, A&A, 699, A311

Marasco, A., Fall, S. M., Di Teodoro, E. M., & Mancera Piña, P. E. 2025, A&A, 695, L23

Marasco, A., Fraternali, F., Posti, L., et al. 2019, A&A, 621, L6

Marasco, A., Posti, L., Oman, K., et al. 2020, A&A, 640, A70

Martinsson, T. P. K., Verheijen, M. A. W., Westfall, K. B., et al. 2013, A&A, 557, A130

Martorano, M., van der Wel, A., Baes, M., et al. 2024, ApJ, 972, 134

Martorano, M., van der Wel, A., Bell, E. F., et al. 2023, ApJ, 957, 46

McGaugh, S. S. 2012, AJ, 143, 40

Mercier, W., Epinat, B., Contini, T., et al. 2023, A&A, 677, A143

Mo, H. J., Mao, S., & White, S. D. M. 1998, MNRAS, 295, 319

Mogotsi, K. M. & Romeo, A. B. 2019, MNRAS, 489, 3797

Moster, B. P., Somerville, R. S., Maulbetsch, C., et al. 2010, ApJ, 710, 903

Navarro, J. F., Frenk, C. S., & White, S. D. M. 1997, ApJ, 490, 493

Nelson, D., Springel, V., Pillepich, A., et al. 2019, Computational Astrophysics and Cosmology, 6, 2

Nelson, E. J., van Dokkum, P. G., Brammer, G., et al. 2012, ApJ, 747, L28

Nelson, E. J., van Dokkum, P. G., Förster Schreiber, N. M., et al. 2016, ApJ, 828, 27

Obreschkow, D. & Glazebrook, K. 2014, ApJ, 784, 26

Obreschkow, D., Meyer, M., Popping, A., et al. 2015, in Advancing Astrophysics with the Square Kilometre Array (AASKA14), 138

Oliphant, T. E. 2007, Computing in Science Engineering, 9, 10

Paquereau, L., Laigle, C., McCracken, H. J., et al. 2025, arXiv e-prints, arXiv:2501.11674

Pedrosa, S. E. & Tissera, P. B. 2015, A&A, 584, A43

Peebles, P. J. E. 1969, ApJ, 155, 393

Pellizza, D., Lemaux, B. C., Tomczak, A. R., et al. 2019, MNRAS, 482, 3514

Peng, C. Y., Ho, L. C., Impey, C. D., & Rix, H.-W. 2010, AJ, 139, 2097

Pezzulli, G., Fraternali, F., & Binney, J. 2017, MNRAS, 467, 311

Ponomareva, A. A., Verheijen, M. A. W., Peletier, R. F., & Bosma, A. 2017, MNRAS, 469, 2387

Posti, L., Fraternali, F., Di Teodoro, E. M., & Pezzulli, G. 2018, A&A, 612, L6

Posti, L., Fraternali, F., & Marasco, A. 2019a, A&A, 626, A56

Posti, L., Marasco, A., Fraternali, F., & Famaey, B. 2019b, A&A, 629, A59

Price, S. H., Kriek, M., Shapley, A. E., et al. 2016, ApJ, 819, 80

Reyes, R., Mandelbaum, R., Gunn, J. E., et al. 2012, MNRAS, 425, 2610

Reyes, R., Mandelbaum, R., Gunn, J. E., Pizagno, J., & Lackner, C. N. 2011, MNRAS, 417, 2347

Rizzo, F., Kohandel, M., Pallottini, A., et al. 2022, A&A, 667, A5

Rizzo, F., Roman-Oliveira, F., Fraternali, F., et al. 2023, A&A, 679, A129

Rodriguez-Gómez, V., Genel, S., Fall, S. M., et al. 2022, MNRAS, 512, 5978

Rodriguez-Gómez, V., Sales, L. V., Genel, S., et al. 2017, MNRAS, 467, 3083

Romanowsky, A. J. & Fall, S. M. 2012, ApJS, 203, 17

Romeo, A. B., Agertz, O., & Renaud, F. 2020, MNRAS, 499, 5656

Romeo, A. B., Agertz, O., & Renaud, F. 2023, MNRAS, 518, 1002

Rowland, L. E., Hodge, J., Bouwens, R., et al. 2024, MNRAS, 535, 2068

Sales, L. V., Navarro, J. F., Schaye, J., et al. 2009, MNRAS, 399, L64

Schombert, J., McGaugh, S., & Lelli, F. 2022, AJ, 163, 154

Scoville, N., Aussel, H., Brusa, M., et al. 2007, ApJS, 172, 1

Sharma, G., Salucci, P., Harrison, C. M., van de Ven, G., & Lapi, A. 2021, MNRAS, 503, 1753

Sharma, G., Upadhyaya, V., Salucci, P., & Desai, S. 2024, A&A, 689, A318

Shuntov, M., Ilbert, O., Toft, S., et al. 2025, A&A, 695, A20

Simons, R. C., Peebles, M. S., Tumlinson, J., et al. 2025, ApJ, 988, 250

Somerville, R. S., Barden, M., Rix, H.-W., et al. 2008, ApJ, 672, 776

Somerville, R. S., Behroozi, P., Pandya, V., et al. 2018, MNRAS, 473, 2714

Somerville, R. S., Gabrielpillai, A., Hadzhiyska, B., & Genel, S. 2025, arXiv e-prints, arXiv:2502.03679

Speagle, J. S. 2020, MNRAS, 493, 3132

Stanway, E. R. & Eldridge, J. J. 2018, MNRAS, 479, 75

Stevens, A. R. H., Croton, D. J., & Mutch, S. J. 2016, MNRAS, 461, 859

Stott, J. P., Swinbank, A. M., Johnson, H. L., et al. 2016, MNRAS, 457, 1888

Suess, K. A., Bezanson, R., Nelson, E. J., et al. 2022, ApJ, 937, L33

Swaters, R. A. 1999, PhD thesis, Kapteyn Astronomical Institute, University of Groningen

Sweet, S. M., Fisher, D. B., Savorgnan, G., et al. 2019, MNRAS, 485, 5700

Sweet, S. M., Glazebrook, K., Obreschkow, D., et al. 2020, MNRAS, 494, 5421

Swinbank, A. M., Harrison, C. M., Trayford, J., et al. 2017, MNRAS, 467, 3140

Tacconi, L. J., Genzel, R., & Sternberg, A. 2020, ARA&A, 58, 157

Taylor, M. B. 2005, in Astronomical Society of the Pacific Conference Series, Vol. 347, Astronomical Data Analysis Software and Systems XIV, ed. P. Shopbell, M. Britton, & R. Ebert, 29

Teklu, A. F., Remus, R.-S., Dolag, K., et al. 2015, ApJ, 812, 29

Tiley, A. L., Bureau, M., Cortese, L., et al. 2019, MNRAS, 482, 2166

Tully, R. B. & Fisher, J. R. 1977, A&A, 500, 105

Übler, H., Förster Schreiber, N. M., Genzel, R., et al. 2017, ApJ, 842, 121

van den Bosch, F. C., Burkert, A., & Swaters, R. A. 2001, MNRAS, 326, 1205

van den Bosch, F. C., Jiang, F., Hearin, A., et al. 2014, MNRAS, 445, 1713

van der Kruit, P. C. 1988, A&A, 192, 117

van der Wel, A., Bell, E. F., Häussler, B., et al. 2012, ApJS, 203, 24

van der Wel, A., Chang, Y.-Y., Bell, E. F., et al. 2014, ApJ, 792, L6

van Dokkum, P. G. & Franx, M. 1996, MNRAS, 281, 985

van Dokkum, P. G. & Franx, M. 2001, ApJ, 553, 90

Virtanen, P., Gommers, R., Oliphant, T. E., et al. 2020, Nature Methods, 17, 261

Wang, S., Xu, D., & Lu, S. 2025, ApJ, 986, 85

Wang, S., Xu, D., Lu, S., et al. 2022, MNRAS, 509, 3148

White, S. D. M. 1984, ApJ, 286, 38

White, S. D. M. & Rees, M. J. 1978, MNRAS, 183, 341

Wilman, D. J., Fossati, M., Mendel, J. T., et al. 2020, ApJ, 892, 1

Wisnioski, E., Förster Schreiber, N. M., Fossati, M., et al. 2019, ApJ, 886, 124

Wisnioski, E., Förster Schreiber, N. M., Wuyts, S., et al. 2015, ApJ, 799, 209

Yang, H., Liao, S., Fattah, A., et al. 2024, MNRAS, 535, 1394

Appendix A: Kinematic modelling

Given the relatively short extent of the H α emission in the KROSS and KMOS^{3D} data compared to the PSF, the observations can suffer from strong beam smearing (Swaters 1999; Di Teodoro & Fraternali 2015). To deal with this, our kinematic approach differs from those conventionally used in other studies of the KROSS and KMOS^{3D} samples, such as fitting velocity fields or extracting 1D kinematic profiles and applying simplified beam-smearing corrections a posteriori (e.g. Burkert et al. 2016; Harrison et al. 2017; Swinbank et al. 2017). Such approaches may result in an underestimation of the rotational velocities and an overestimation of the velocity dispersion (Di Teodoro & Fraternali 2015; Rizzo et al. 2022; de Araujo-Carvalho et al. 2025). Instead, we use the software ^{3D}Barolo¹⁰ (Di Teodoro & Fraternali 2015), which performs forward-modelling on the whole H α data cube and, thanks to a convolution with the observational PSF (described by a 2D Gaussian), mitigates the effects of beam-smearing. ^{3D}Barolo has been used to fit different emission lines at different redshifts (e.g. Fraternali et al. 2021; Sharma et al. 2021; Di Teodoro & Peek 2021; Rizzo et al. 2023; Mancera Piña et al. 2024; Rowland et al. 2024; Liu et al. 2025), and crucially, it has been tested extensively with artificially-degraded H α observations of nearby galaxies and realistic mock galaxies drawn from simulations, showing that it can correctly recover the rotational speed even when the spatial resolution is sparse and reduced down to several kpc (e.g. Di Teodoro & Fraternali 2015; Di Teodoro et al. 2016; Mancera Piña et al. 2020; Rizzo et al. 2022).

During our kinematic modelling, some parameters are kept fixed, while others are free to vary. The parameters that remained fixed to our input values are the inclination (fixed to the inclination derived from the GALFIT fits to the JWST/HST data) and redshift (taken from the KROSS and KMOS^{3D} databases). Additionally, ^{3D}Barolo estimates the centre based on the total H α intensity map. The parameters being fitted are the position angle, the systemic velocity (V_{sys}), the rotational velocity ($V_{\text{rot},\text{H}\alpha}$), and the gas velocity dispersion ($\sigma_{\text{H}\alpha}$). The position angle is given an initial value based on the GALFIT measurement and allowed to vary within the uncertainties (regularised with a straight line, see Di Teodoro & Fraternali 2015) to account for small misalignments resulting from the different spatial resolutions and PSFs. While we specify the redshift, we consider V_{sys} a free parameter to account for differences between the values reported by the KROSS and KMOS^{3D} teams (based on Gaussian fits to the emission lines) and the more sophisticated kinematic V_{sys} , which can be aggravated by the relatively low spectral resolution of the data and the noise. Finally, $\sigma_{\text{H}\alpha}$ and especially $V_{\text{rot},\text{H}\alpha}$ are the main parameters we are interested in.

Before the fitting, we need to specify a few additional settings in the ^{3D}Barolo configuration. First, the ring separation (i.e. the radial separation of our rotation curves). As a compromise between obtaining a good sampling of the rotation curve and avoiding strong correlations between pixels, we adopt a ring separation of FWHM/2, where FWHM is the reported FWHM of the PSF by the KROSS and KMOS^{3D} collaborations. Second, there is the mask: we follow Mancera Piña et al. (2025) and derive first an automatic mask using the SEARCH task of ^{3D}Barolo, which we then enlarge spatially by 2 pixels; this allows us to include low S/N regions while minimising the contribution from the noisy background. With this, we proceed to obtain our kinematic models using a $\cos(\theta)$ weighting scheme and azimuthal normalisation (see Di Teodoro & Fraternali 2015 and its documentation for details). We have built mock data cubes that mimic KMOS IFU data and find that the intrinsic $V_{\text{rot},\text{H}\alpha}$ and $\sigma_{\text{H}\alpha}$ are well recovered using this scheme.

After excluding galaxies for which reliable kinematic modelling could not be obtained (e.g. when emission across channel maps cannot be reproduced, PV diagrams do not indicate a rotating disc, or the data are strongly asymmetric; see Rizzo et al. 2022), our final sample consists of 43 disc galaxies with robust kinematic models. Figure A.1 presents six representative examples of our kinematic data and models across the M_* range, while Figure A.2 shows the corresponding rotation curves. The sample is composed of regularly rotating, rotation-dominated discs, with a median $\sigma_{\text{med},\text{H}\alpha}$ of 40 km/s and a median $V_f/\sigma_{\text{med},\text{H}\alpha}$ of 5 (Fig. 1).

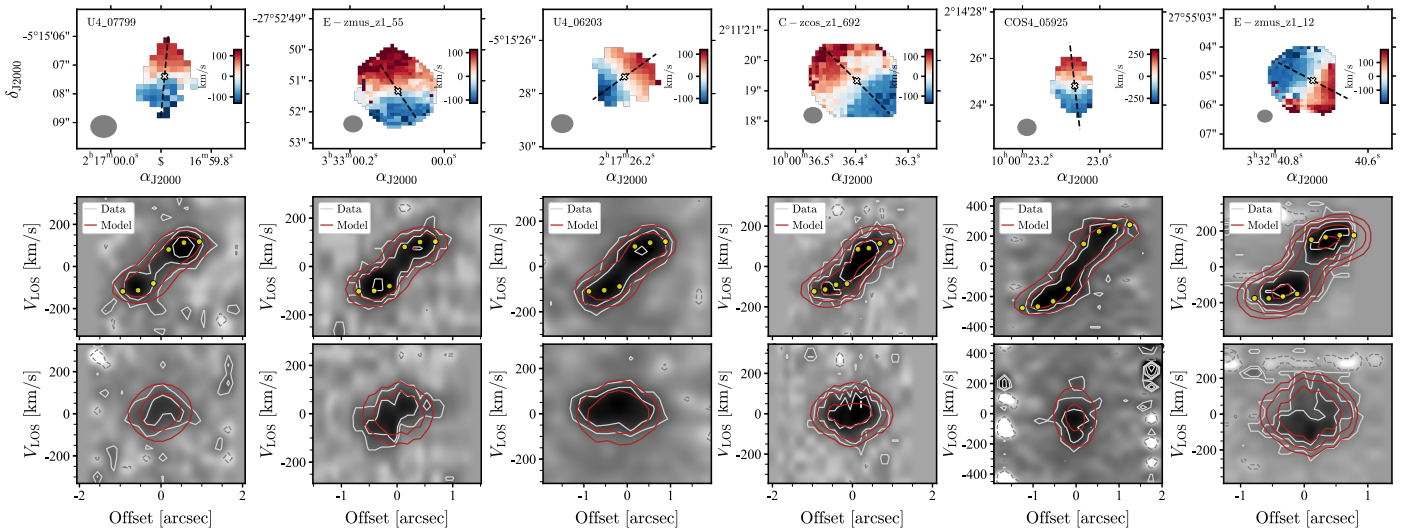


Fig. A.1: Examples of the kinematic data and models for our sample covering our M_* range. We show their velocity field (top), major-axis PV (middle), and minor-axis PV (bottom). The top panels also show the centre (white cross), kinematic major axis (black dashed line), and PSF (grey ellipse). In the PV plots, data are shown in a grey background and black contours (grey for negative values), and the best-fitting ^{3D}Barolo model is in red. Line-of-sight velocities are shown in yellow. Contours are at $-2, 2, 2^n \sigma_{\text{r.m.s.}}$.

¹⁰ v1.7, <https://editeodoro.github.io/Bbarolo/>

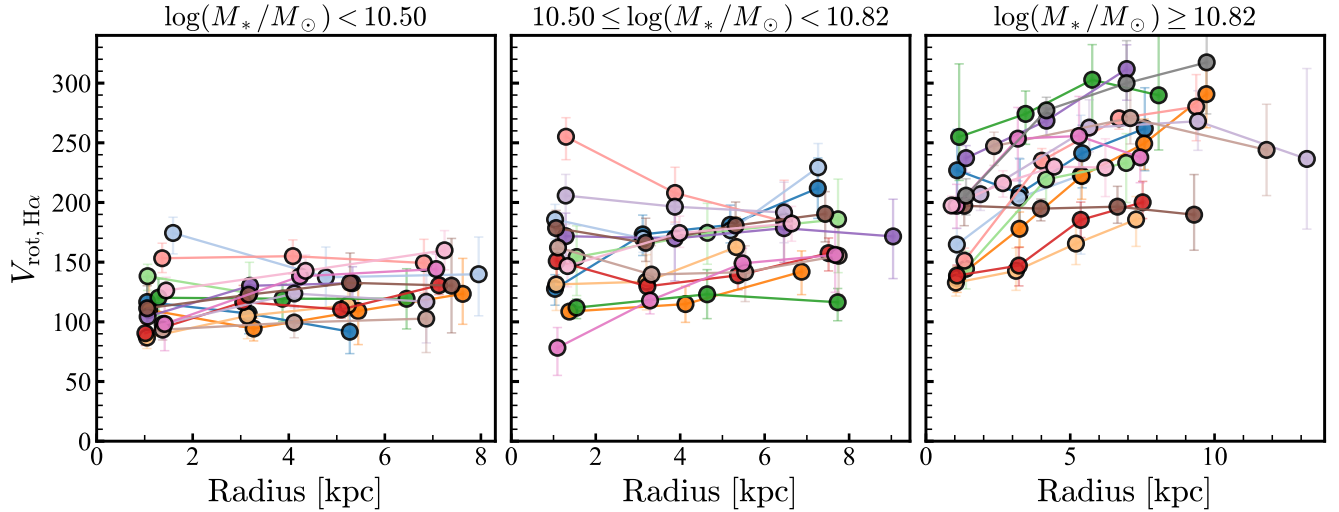


Fig. A.2: $\text{H}\alpha$ rotation curves of our galaxy sample, derived with ${}^3\text{D}\text{Barolo}$. Galaxies are divided into three bins according to their stellar mass. All our rotation curves and velocity dispersion measurements are available upon request.

In Sect. 4.1, we present our $z = 0.9$ TFR and FR. Upon close inspection of the data, we notice that there is a trend with V_f/σ_{med} , such that at fixed M_* galaxies with higher V_f/σ_{med} have also a higher V_f and j_* . This is shown in Fig. A.3. Similar trends for the FR at $z \sim 1 - 3$ have been reported before (e.g. Burkert et al. 2016; Harrison et al. 2017; Bouché et al. 2021), and we have now confirmed them with accurate kinematic modelling that self-consistently derives the rotation and velocity dispersions.

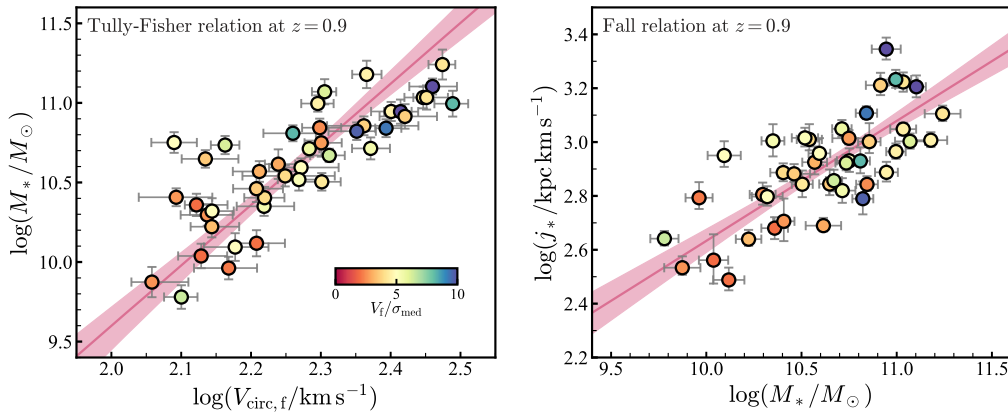


Fig. A.3: Dependency of the $z = 0.9$ TFR and FR on V_f/σ_{med} . The pink solid curves and shaded band represent our best-fit relations and their 1σ confidence bands.

Appendix B: Calibrating our measurement technique with galaxies at $z \sim 0$

Given our methodology presented in Sect. 3, it is particularly crucial to ensure that we can recover the characteristic velocities at the flat part of our rotation curves (either $V_{\text{circ},f}$ or V_f). To ensure that our methods are reliable, we tested and calibrated them on a sample of nearby disc galaxies (which have a similar Sérsic distribution as our sample) with detailed and accurate measurements of V_f and j_* based on high-resolution rotation curves and NIR photometry. Specifically, we used the SPARC compilation (Lelli et al. 2016), which is also the sample used by Marasco et al. (2025) to derive the $z = 0$ TFR and FR we compare against in Sect. 4.2. The SPARC galaxies have V_f and j_* measurements from Lelli et al. (2016), and Posti et al. (2018) and Mancera Piña et al. (2021a), respectively, which were derived from the data without the use of any functional forms.

We have corroborated that our approach is robust as follows. First, we take the SPARC rotation curves and cut them so that they do not extend more than four times their effective radius (derived from Sérsic fits to the SPARC surface brightness profiles). Second, we downsample the rotation curves by using linear interpolation to extract rotational speeds at only four radii (note that the results remain unchanged when performed at three or five radii). These two steps ensure that the downsampled rotation curves resemble those from the $z = 0.9$ $\text{H}\alpha$ data. Next, we fit the rotation curves with arctan profiles as in Sect. 3.

From empirical tests, we find that the best way to retrieve the characteristic flat velocity from the low-resolution data is to evaluate the best-fitting arctan model at $R = 2 R_{\text{eff}}$ for galaxies with $V_a > 100 \text{ km/s}$ and $R = 3 R_{\text{eff}}$ for galaxies with $V_a < 100 \text{ km/s}$. As shown in the left panel of Fig. B.1, this results in an excellent agreement with the high-resolution measurements, with only a negligible offset. Similarly, we measure j_* sampling Eq. 6 as described in the main text, and compare our values against the high-resolution estimates (right panel in Fig. B.1). Once again, there is an excellent agreement, with low residuals and scatter. From this discussion, we conclude that our methodology for deriving the characteristic flat velocity and j_* is robust. We have also double-

checked that the $z = 0$ TFR and FR re-derived with this technique have slopes and intercepts compatible with those inferred by Marasco et al. (2025).

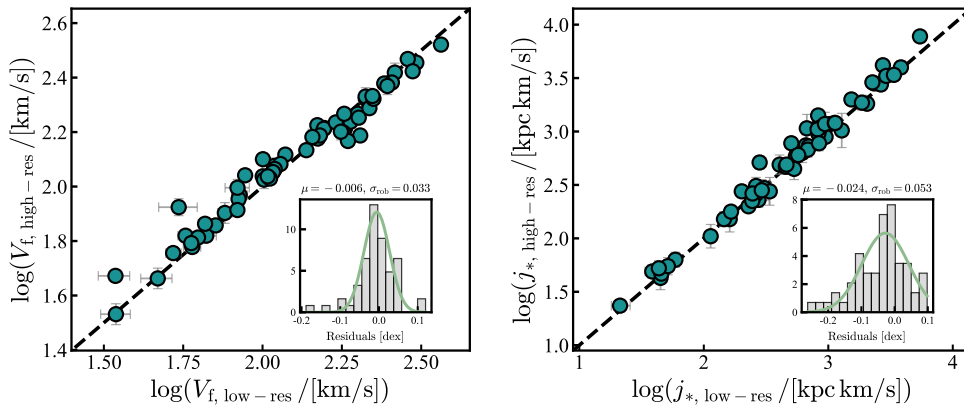


Fig. B.1: Calibration of our V_f (left) and j_* (right) estimates. The figure compares the measurements at $z = 0$ obtained from high-resolution kinematics with those from downsampled rotation curves, which have a low spatial sampling similar to the $z = 0.9$ H α data. The agreement is excellent, as highlighted by the residuals shown in the insets.

Appendix C: Abundance-matching expectations

As discussed in the main text, the f_M values found at $z = 0.9$ (but also at $z = 0$) are different from those expected from Moster et al. (2010) based on abundance-matching techniques. To visualise the level of this disagreement, in Fig. C.1 we compare the observed TFRs with those implied by the $f_M - M_*$ relations from Moster et al. (2010), after assuming the same f_V as in Sect. 5.1, i.e. solving Eq. 15 for the abundance-matching TFRs.

At low z (note that here we have assumed $V_{\text{circ},f} = V_f$) we can see discrepancies previously known in the literature, namely some dwarfs with lower M_* than expected (the ‘baryon deficient dwarfs’ from Mancera Piña et al. 2025, see also Forbes & Gannon 2024), and some massive spirals with higher M_* than predicted by abundance matching (e.g. Posti et al. 2019a; Marasco et al. 2020; Di Teodoro et al. 2023; Mancera Piña et al. 2022). Our observations show that the discrepancies with abundance matching become much more dramatic at $z = 0.9$, with the abundance-matching TFR being about 0.7 dex too low in $\log(M_*)$ or 0.25 dex in $\log(V_f)$, and with a curvature not evident in the data. Alternatively, setting $f_V = 0.8$ would make the abundance-matching expectations consistent with the data, but it is unlikely that such a low value is valid for our M_* range (McGaugh 2012).

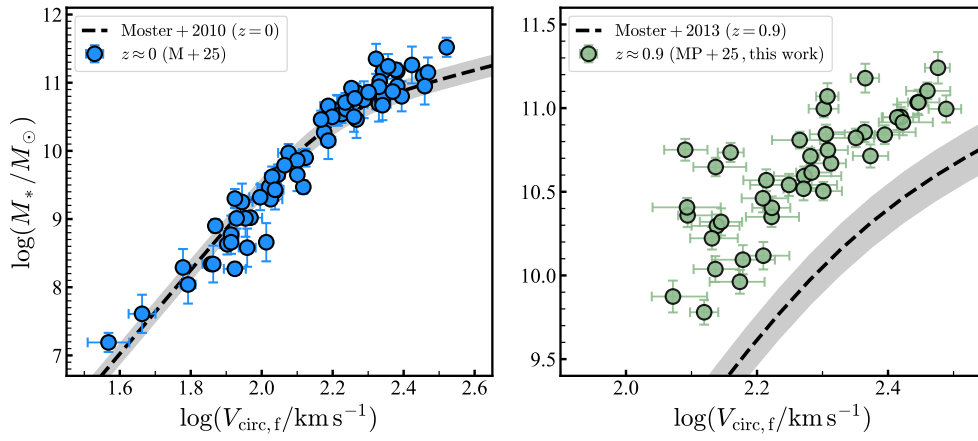


Fig. C.1: Observed TFRs against the predictions from abundance matching, after assuming the f_V discussed in the main text. Note the differences in the axes span.

Appendix D: Sample and main physical parameters

Table D.1: Main parameters of our galaxy sample.

Name	z	$\log(M_*/M_\odot)$	$\delta_{\log(M_*/M_\odot)}$	j_*			$V_{\text{circ,f}}$			$V_f/\sigma_{\text{med,H}\alpha}$
(1)	(2)	(3)	(4)	p16	p50	p84	p16	p50	p84	(11)
C-HiZ_z1_245	0.833	10.50	0.06	620.17	697.33	778.75	188.02	200.13	212.63	4.3
C-HiZ_z1_258	0.838	10.71	0.05	1043.03	1119.82	1204.33	188.77	192.06	198.48	5.7
C-HiZ_z1_289	0.843	10.65	0.06	632.10	698.67	785.08	125.69	136.34	151.19	3.6
C-zcos_z1_182	0.970	10.95	0.06	711.37	771.99	841.24	234.93	251.63	268.57	4.6
C-zcos_z1_188	0.880	10.04	0.08	291.42	364.33	444.86	124.25	134.46	145.98	2.0
C-zcos_z1_189	0.938	10.86	0.06	905.49	1003.39	1162.25	202.03	229.95	271.30	3.7
C-zcos_z1_192	0.914	10.57	0.07	754.47	841.57	955.04	148.65	162.92	183.53	3.1
C-zcos_z1_198	0.959	10.84	0.06	1215.18	1280.64	1355.75	238.55	247.41	259.88	9.3
C-zcos_z1_202	0.841	10.84	0.06	657.38	696.55	745.25	187.24	198.79	212.85	2.5
C-zcos_z1_484	0.855	11.10	0.05	1460.18	1604.43	1759.81	266.29	288.37	311.64	12.4
C-zcos_z1_5	0.869	10.82	0.06	533.55	616.09	707.02	203.68	224.60	238.76	9.7
C-zcos_z1_611	0.835	10.75	0.07	770.92	851.95	942.51	113.74	122.98	132.21	5.0
C-zcos_z1_619	0.838	10.59	0.06	816.49	907.99	1026.06	167.18	186.92	210.09	5.0
C-zcos_z1_621	0.919	10.35	0.06	876.00	1010.13	1154.16	150.52	165.46	181.88	5.4
C-zcos_z1_659	0.982	10.36	0.07	434.12	478.96	523.89	127.30	132.39	145.95	2.0
C-zcos_z1_660	0.929	10.73	0.06	783.93	836.18	894.51	138.66	145.50	152.36	6.2
C-zcos_z1_690	0.925	10.71	0.07	591.24	660.30	730.56	220.71	235.15	250.11	5.5
C-zcos_z1_692	0.927	11.00	0.05	864.57	921.74	985.93	186.75	197.53	207.85	4.5
C-zcos_z1_698	0.927	10.81	0.05	761.27	850.90	949.66	164.26	181.94	195.74	8.2
C-zcos_z1_726	0.928	10.67	0.04	654.08	718.95	786.09	192.24	205.15	215.64	6.4
C-zcos_z1_793	0.885	10.41	0.06	421.85	507.93	606.71	108.54	123.83	138.58	2.7
COS4_05925	0.799	11.03	0.07	1056.84	1117.08	1178.54	270.52	279.69	289.03	4.5
COS4_06487	0.907	11.24	0.09	1194.21	1274.12	1362.13	284.26	297.95	310.59	4.2
COS4_16172	1.030	11.03	0.08	1532.45	1671.95	1807.81	262.11	282.77	302.68	4.2
COS4_17628	0.907	11.07	0.08	942.80	1005.94	1073.15	193.59	202.04	209.76	6.2
COS4_23890	0.852	10.95	0.08	2016.41	2213.38	2431.61	245.49	259.50	274.59	12.7
C-zcos_z1_675	0.891	10.91	0.08	1488.39	1625.61	1798.41	241.26	263.33	291.14	3.7
C-zcos_z1_693	0.925	10.30	0.07	583.29	638.75	703.67	125.15	137.19	148.70	2.6
E-zmus_z1_119	0.841	10.75	0.09	978.12	1032.94	1104.22	188.77	199.82	213.29	2.7
E-zmus_z1_12	0.976	11.18	0.09	956.32	1015.91	1085.51	220.99	232.06	243.44	4.6
E-zmus_z1_148	0.840	10.12	0.08	280.25	307.62	340.04	150.02	161.39	176.51	2.1
E-zmus_z1_166	0.975	10.62	0.09	465.55	489.33	521.80	165.74	173.41	183.11	3.0
E-zmus_z1_202	0.861	9.78	0.07	412.20	437.90	466.65	118.77	125.95	132.66	6.5
E-zmus_z1_24	0.823	10.40	0.07	713.44	770.29	831.07	154.63	165.75	176.59	3.9
E-zmus_z1_49	0.982	10.54	0.07	927.67	1022.75	1156.29	152.38	177.39	206.40	3.9
E-zmus_z1_55	0.885	10.32	0.08	578.56	627.25	682.82	129.22	139.36	149.34	5.0
E-zmus_z1_65	0.842	9.96	0.07	561.49	621.02	704.09	130.39	147.22	161.00	2.2
E-zmus_z1_70	0.858	10.22	0.07	410.94	435.92	470.45	129.53	139.24	151.83	3.3
E-zmus_z1_86	0.841	9.87	0.10	320.72	341.47	374.75	106.57	114.30	128.05	2.6
U4_06203	0.803	10.52	0.07	960.35	1036.43	1125.88	172.68	185.59	201.76	5.2
U4_07799	0.809	10.09	0.09	804.60	891.60	1000.24	134.90	150.42	166.94	5.0
U4_22990	0.787	10.99	0.08	1585.61	1706.51	1847.94	289.62	308.19	323.95	8.1
U4_34173	0.896	10.46	0.08	709.28	762.21	825.37	148.93	161.36	175.47	3.6

Notes. Column (1) gives the galaxy ID as provided by the KROSS and KMOS^{3D} teams. Column (2) is the redshift from the KROSS and KMOS^{3D} catalogues. Columns (3) and (4) quote the stellar masses and their uncertainties. Columns (5) to (7) give the 16th, 50th, and 84th percentiles of our j_* estimates. Columns (8) to (10) give the 16th, 50th, and 84th percentiles of $V_{\text{circ,f}}$. Column (11) lists the rotation to dispersion ratio $V_f/\sigma_{\text{med,H}\alpha}$.